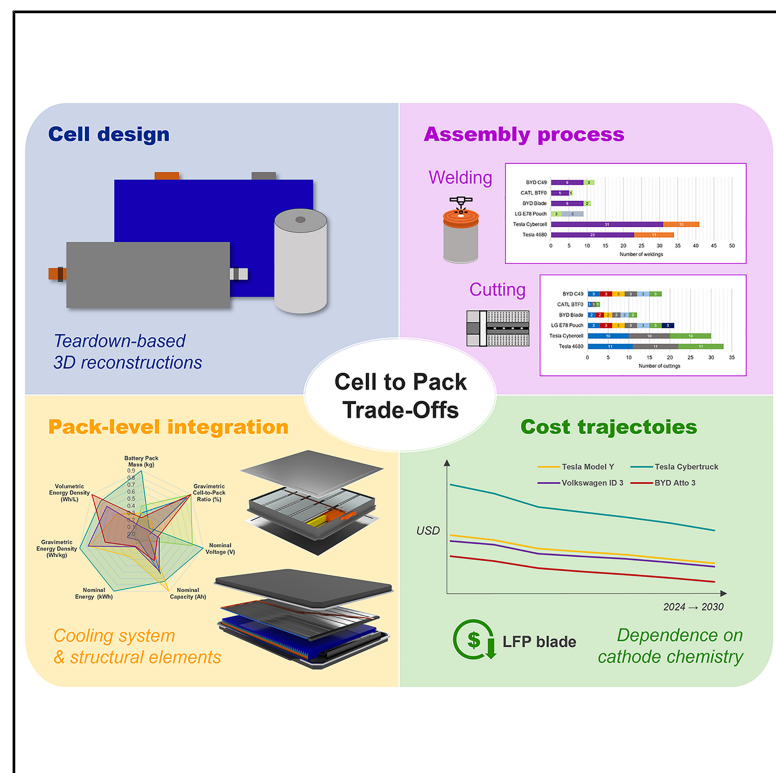


# Design and production trade-offs in lithium-ion batteries from cell formats to electric vehicles

## Graphical abstract



## Authors

Marella De Santis, Irene Giusti, Federico Poli, Luca Piancastelli, Alfredo Liverani

## Correspondence

marella.desantis2@unibo.it

## In brief

De Santis et al. develop a teardown-based benchmarking framework that enables uniform, end-to-end comparison of commercial cylindrical, pouch, and prismatic Li-ion cells from cell level to EV pack. The results quantify format-driven trade-offs in energy density, manufacturability, integration overhead, and projected cost, providing actionable guidance for scalable cell-to-pack design.

## Highlights

- Design, performance, assembly, and pack integration of commercial cells are compared
- Cylindrical and pouch NMC cells optimize active volume allocation with >600 Wh/L
- Blade cells reach high pack volumetric energy density and a GCTP ratio of 75%
- Cost projections show blade-based packs remain the lowest cost option to 2030



## Article

# Design and production trade-offs in lithium-ion batteries from cell formats to electric vehicles

Marella De Santis,<sup>1,3,\*</sup> Irene Giusti,<sup>1</sup> Federico Poli,<sup>2</sup> Luca Piancastelli,<sup>1</sup> and Alfredo Liverani<sup>1</sup>
<sup>1</sup>Department of Industrial Engineering, Alma Mater Studiorum - University of Bologna, 40136 Bologna, Italy

<sup>2</sup>Coesia Engineering Center, 40133 Bologna, Italy

<sup>3</sup>Lead contact

\*Correspondence: [marella.desantis2@unibo.it](mailto:marella.desantis2@unibo.it)
<https://doi.org/10.1016/j.xcrp.2026.103162>

## SUMMARY

Sustainable energy systems demand energy-dense, scalable, manufacturable, and readily integrable lithium-ion batteries, yet available literature provides fragmented comparisons of commercial cell formats. Here we report a unified, industrially grounded benchmarking framework for cylindrical, pouch, and prismatic cells using parameters selected for high-fidelity derivability across formats and direct relevance to manufacturing and system integration. At cell level, active/inactive volume allocation, gravimetric and volumetric energy densities, and assembly complexity are quantified. At pack level, we evaluate nominal voltage and capacity, pack energy, gravimetric cell-to-pack ratio, cooling, and structural integration descriptors. Chemistry-dependent single-cell and pack-scaled costs are estimated from prospective cost trajectories. Fast-charging capability, resistance growth and aging, and quantitative thermal performance are excluded due to noncomparable datasets; pack thermal implications are discussed qualitatively. The framework shows cylindrical lithium nickel manganese cobalt oxide cells maximizes cell-level energy density but increases structural overhead, whereas lithium iron phosphate blade designs maximize cell-to-pack ratio, pack volumetric energy, and cost competitiveness.

## INTRODUCTION

Modern electrochemical energy storage is dominated by lithium-ion batteries, which enable applications ranging from consumer electronics to electric vehicles (EVs)<sup>1,2</sup> and renewable-energy systems.<sup>3,4</sup> Their performance is determined by specific energy and power, cycle life, and safety. Specific energy depends on electrode materials and their micro- and nano-structural properties, while specific power is governed by electrode conductivity, reaction kinetics, ionic transport, and electrolyte behavior. Cycle life remains a key constraint, as degradation depends strongly on operating conditions,<sup>5</sup> while safety concerns persist due to risks of thermal runaway triggered by overheating, overcharging, or internal short circuits.<sup>4,6–8</sup>

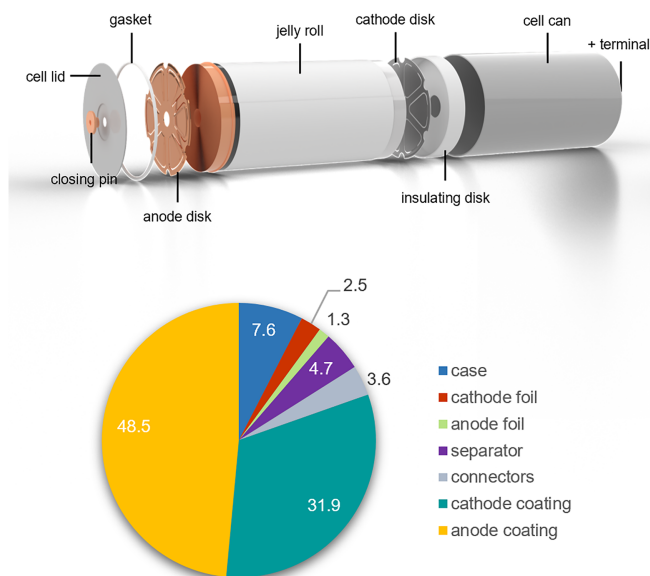
The structure of current lithium-ion cells is well established: graphite anodes and metal-oxide or phosphate cathodes are separated by a liquid electrolyte and enclosed in rigid or laminated housings.<sup>4,9–11</sup> While electrode manufacturing and cell finishing strongly influence electrochemical and thermal behavior, the cell format has a decisive role at the product level, particularly in EV battery-pack integration.<sup>11,12</sup> Each format presents distinct advantages and trade-offs: large-format cylindrical cells employ a wound structure within a robust can, offering mechanical stability and high manufacturing throughput<sup>13–15</sup>; prismatic cells use a flat-wound or stacked electrode arrangement in a

rectangular housing, improving packing efficiency and reducing the number of cell-to-cell connections<sup>16–18</sup>; pouch cells, based on stacked electrodes enclosed in a laminated aluminum-polymer film, minimize weight and achieve high volumetric utilization, though at the cost of low mechanical rigidity.<sup>19</sup> The rapid expansion of gigafactories, driven by decarbonization targets and the transition to electric mobility, has brought manufacturing scalability to the forefront. High-automation, high-productivity environments demand cell formats that balance energy density, safety, thermal behavior, and ease of production. Understanding which design choices facilitate or hinder scalable manufacturing is therefore essential for identifying suitable technologies for next-generation EVs.<sup>20,21</sup>

This work contributes to the growing literature<sup>14,19,22–25</sup> investigating format-specific implications for mass production and system integration. By combining teardown-based geometric reconstruction, volumetric decomposition, and analysis of assembly workflows, the study provides a comparative evaluation of six commercial cell formats representative of current industrial practices. The assessment spans metrics such as energy and power density, component-level volumetric allocation, and manufacturing process intensity, highlighting how design choices influence both performance and producibility. Because cells ultimately function within battery packs, the analysis extends to pack-level architecture, examining how cell geometry



### A Tesla 4680 Gen 1



### B Tesla 4680 Cybercell

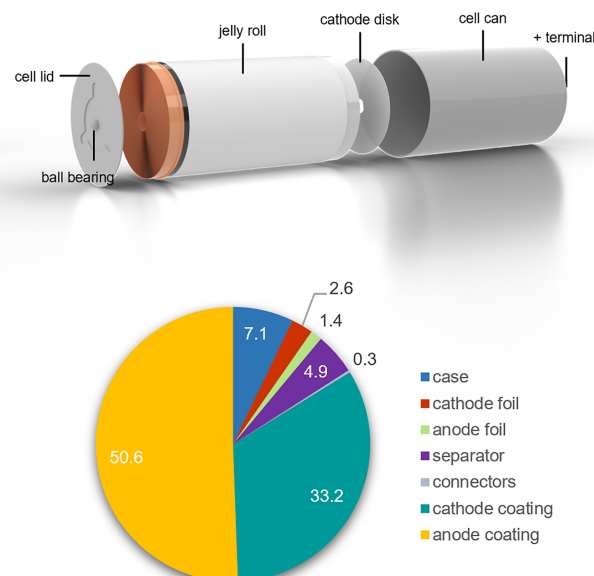


**Figure 1. Cell component layout and internal volume distribution in cylindrical cells**

Exploded 3D reconstructions show the main components of each cylindrical lithium-ion cell, including casing, electrodes, separator, and connectors. The pie charts below quantify the internal volume allocation among active and inactive components, highlighting differences in material distribution and packaging efficiency between the two architectures.

(A) Tesla 4680 Gen 1 cell.

(B) Tesla 4680 Cybercell.

affects integration and overall energy availability. The study also incorporates an economic dimension, linking cell architecture and volume utilization to projected cost trends, with the aim of identifying formats that offer both technical and economic advantages under gigafactory conditions. Identifying the trade-offs associated with cell format is therefore not only a matter of electrochemical performance but a strategic requirement for minimizing production bottlenecks, managing thermal risk, and reducing cost per kWh in high-volume manufacturing environments. This integrated perspective could support informed decision-making in the development of future lithium-ion technologies for large-scale electrification.

## RESULTS AND DISCUSSION

This section first compares the reconstructed cell architectures and assembly process flows across formats, then reports the resulting cell-level energy and volume metrics. It then extends the analysis to pack-level cell packaging strategies, cooling systems, and cost projections to identify format-dependent trade-offs.

### 4680 cylindrical cells

Tesla's recent 4680 cell format (46 mm in diameter and 80 mm in height) has a wound electrode-separator layered structure enclosed in rigid cases. The low production costs and fast assembly make them ideal for a wide range of applications, including consumer electronics, hybrid (HEVs), and EVs.<sup>26</sup> One of the

main advantages is their durable hard case, which offers strength. The rigid housing helps constrain the jelly-roll expansion due to swelling phenomena, by maintaining consistent electrode pressure.<sup>10</sup> This new cell format offers an internal volume that is 5.5 times greater than that previously used in EV<sup>11</sup> 21700 format and 8 times greater than the 18650 format. Unveiling the second-generation 4680 cell ("Cybercell") in 2024, Tesla continues to make significant advancements in the battery sector.

### 4680 cell design and components

The two generations of Tesla 4680 cylindrical lithium-ion cells share the same external dimensions but differ significantly in structure, materials, and manufacturing, as shown in Figure 1. Cell metrics and specifications are reported in Table S1.

Both cells use a jelly-roll structure of positive and negative electrodes separated by polymer films of PP (polyethylene) or PE (polyethylene), and a central void left by mandrel removal. The 4680 Gen 1 cell (Figure 1A) employs a nickel manganese cobalt oxide (NMC)811 cathode and graphite anode in a nickel-plated steel can that provides mechanical, thermal, and chemical protection. Electrical and thermal connections are achieved through aluminum and copper disks with hexagonal symmetry,<sup>15,27,28</sup> while safety features include an insulating disk element and a plastic gasket, a copper closing pin, and a pressure-release vent with engraved rupture lines.<sup>11,14</sup>

As shown in the cell teardown analysis provided by Munro Live<sup>29</sup> and The Limiting Factor,<sup>30</sup> the second-generation 4680

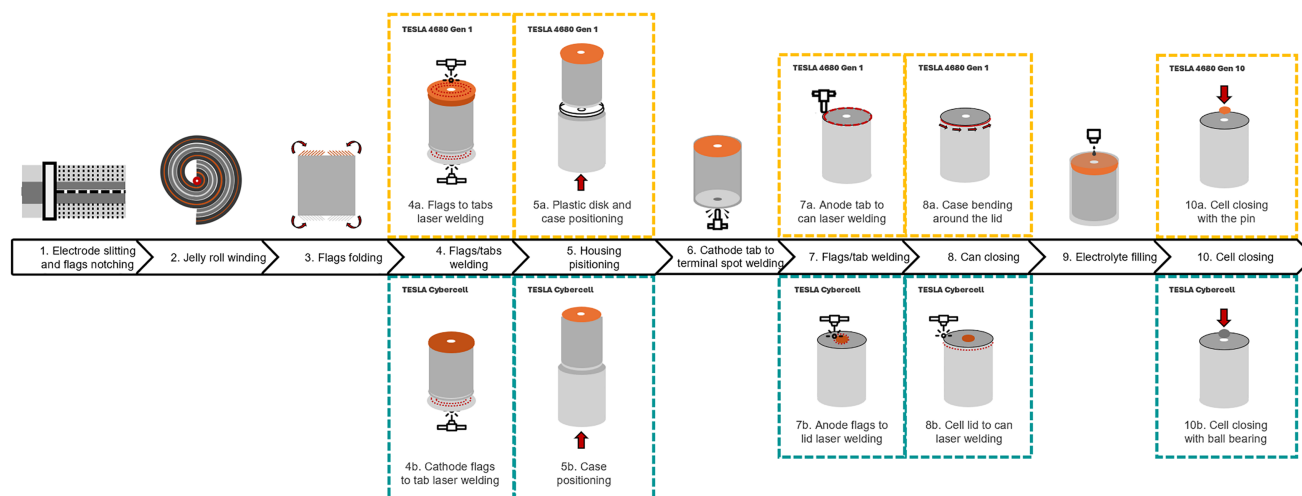


**Figure 2. Cylindrical cell assembly process steps**

The comparison highlights the key differences in tab design, welding sequence, and housing assembly between the architecture of cells. Each schematic step was reconstructed based on descriptions and data from published literature sources.<sup>11,14,27,34–41</sup>

cell, or Cybercell, (Figure 1B) introduces design optimizations to reduce weight, streamline manufacturing, and increase efficiency. The cell's nickel-plated steel housing is approximately 10% thinner and lighter, while the cathode chemistry is upgraded to NMC955. The internal architecture is simplified through direct welding of the negative tabs to the cell cap substituting the copper tab, the use of a thinner and simplified positive aluminum disk, and the removal of the plastic insulating disk. These modifications enhance energy density, thermal management, and production scalability. The venting system has also been redesigned, featuring a bottom-mounted ball bearing that ejects under excess internal pressure to ensure safe pressure release.<sup>30–32</sup>

The main differences in geometry and component dimensions between the two cylindrical cells designed by Tesla are reported in Table S2.

Figure 1 also provides a comparison of the volumetric proportions calculated from the computer-aided design (CAD) models for each component in Tesla's 4680 cylindrical cells (first and second generation), which detailed volumetric values are reported in Table S3. The main observation from the graph is the relatively high volumetric share of the case. This results from the housing with wall thicknesses of 0.5–0.6 mm, significantly thicker than the cases of conventional cylindrical cells,<sup>11,33</sup> to support the larger format.<sup>14</sup> However, this increase is offset by the greater cell volume, which accommodates nearly twice as many electrode windings. Consequently, active materials represent about 80% of the total volume. Other relevant components including the separator, cathode, and anode foil, contribute limited volume but are essential for cell structure and conduction. Additional insulation and welding elements ("connectors" in the graph) further reduce space for active materials. In the Cybercell, the case volume decreases due to thinner walls, while insulation and welding components drop to just 0.3%. This results in a slight increase in active material

to over 83%. These results highlight Tesla's progress in optimizing material use and design in large cylindrical cells.

#### 4680 cell assembly

The assembly process steps of the Tesla 4680 Gen 1 and the "Cybercell" were reconstructed from literature sources<sup>11,14,27,34–41</sup> and are illustrated in Figure 2.

For both cells, the assembly process starts with electrode slitting and notching to form flags in the uncoated regions of the electrode foils by laser cutting. The notches are oriented perpendicular to the winding direction, allowing the formation of multiple current-collecting points after winding.<sup>34,41</sup> The next step is jelly-roll winding, where the cathode, anode, and separator layers are wound together under controlled tension.<sup>42</sup> Subsequently, an automated cutting mechanism employs a cutting knife to trim the material belts, and an adhesive mechanism ensures the proper bonding of the battery cell.<sup>43</sup> After winding, the flags are folded toward the centerline of the electrode roll.<sup>23,41</sup> Subsequently, laser welding of the electrode flags to the collector tabs is performed. In the 4680 Gen 1, both the anode and cathode flags are welded to dedicated metal disks (aluminum-based for the positive and copper-based for the negative),<sup>28</sup> while in the Cybercell only the cathode flags are welded to the tab, eliminating one welding step.<sup>37–39,44</sup> In the 4680 Gen 1 process, the assembly continues with insertion of a plastic disk to avoid short-circuits and placement of the jelly roll into the nickel-plated steel can.<sup>28</sup> The aluminum cathode tab is spot-welded to the positive terminal, and the anode disk is laser-welded directly to the can.<sup>44</sup> The case is then mechanically crimped to seal the top,<sup>11,14</sup> followed by electrolyte filling<sup>11,37</sup> and closing with a pin on the negative side used to seal the filling hole.

In the Cybercell, the jelly roll is directly inserted into the cell can, the bottom of which already includes an insulating layer.<sup>44</sup> The cathode tab is spot-welded to the positive terminal, while the anode tabs are laser-welded directly to the lid. The lid is



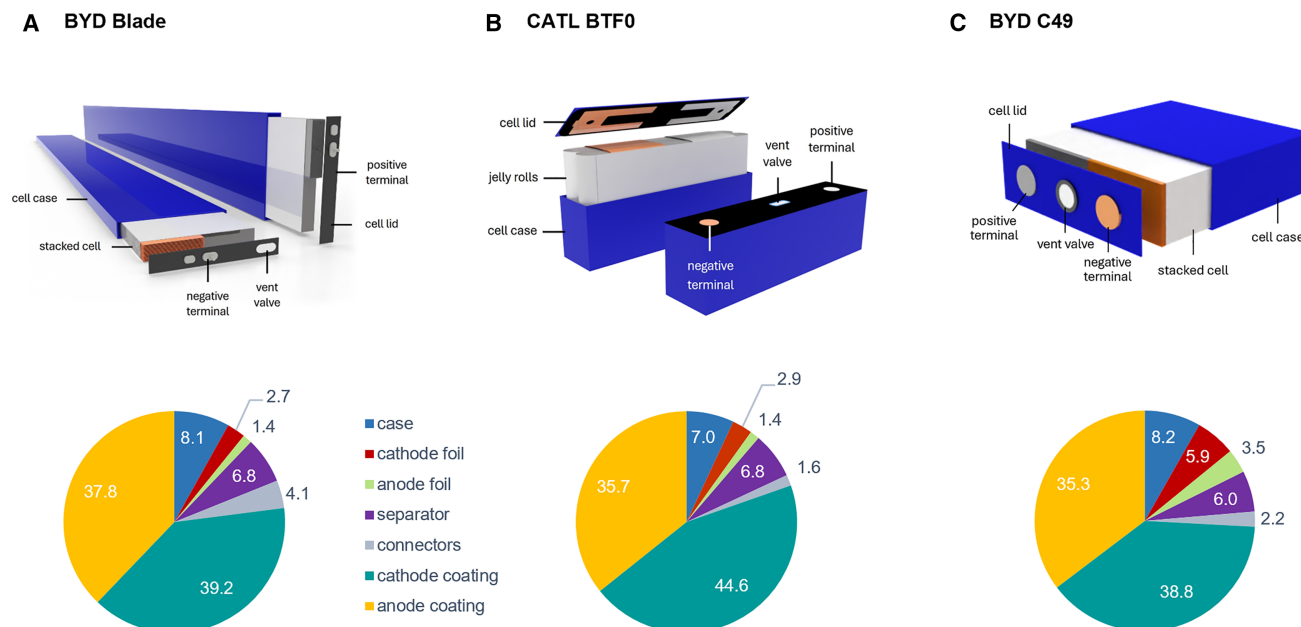


**Figure 3. Cell component layout and internal volume distribution in prismatic cells**

Exploded 3D reconstructions show the main components of each prismatic and blade lithium-ion cell, including casing, electrodes, separator, and connectors. The pie charts below quantify the internal volume allocation among active and inactive components, highlighting differences in material distribution and packaging efficiency between the two architectures.

(A) BYD 138Ah blade cell.  
(B) CATL BTF0 161Ah cell.  
(C) BYD C49 100Ah cell.

then laser-welded to the can, creating a simplified and fully sealed housing.<sup>28</sup> The process concludes with electrolyte filling<sup>11,37</sup> and sealing of the filling hole with a ball bearing that ejects under pressure, working as the primary vent feature.

Compared to the 4680 Gen 1, the Cybercell design reduces the number of welding steps, eliminates the crimping operation, and improves electrical and thermal efficiency through a more direct current path and enhanced housing integrity.

#### Key considerations in 4680 cells

The main differences and improvements from the first to the second generation of 4680 cells are summarized below:

- optimized design structure through components reduction and lighter and thinner case,
- enhanced energy density due to higher active-material fraction and improved cathode chemistry, and
- improved manufacturability (few internal elements and elimination of one welding step in the electrode zone, more scalable industrial process).

#### Prismatic cells

Prismatic cells are typically designed with a rectangular or square shape, offering a compact and easily configurable structure, which allows for good packing efficiency, maximizing the use of available space in battery packs. Cell layout typically consists of stacks of alternating electrode layers separated by a polymeric sheet, all encased in rigid metal or plastic shells.<sup>26,45</sup> To prevent high pressure buildup from cell swelling, many pris-

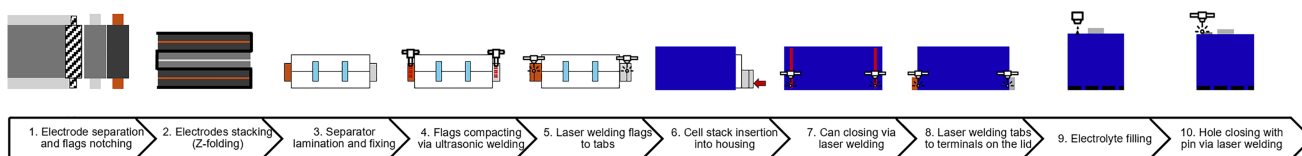
matic cells include a pressure vent port on the lid. They require less “pack hardware” with fewer cell-to-cell connections, potentially leading to higher reliability. Prismatic cells come in various standard formats,<sup>18</sup> but latest trends, such as the BYD Blade, favor longer and narrower cells.

#### Prismatic cells design and components

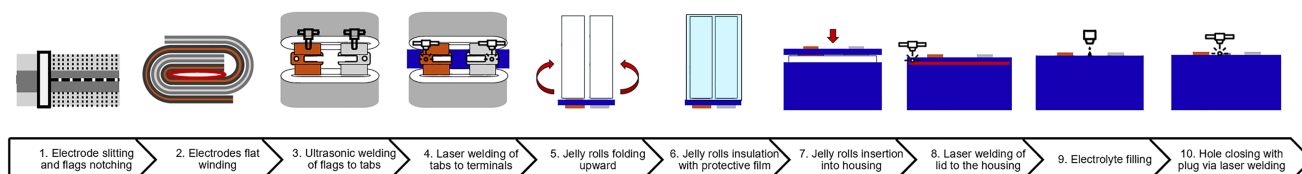
The study focuses on three commercial lithium iron phosphate (LFP) prismatic battery cells, each featuring distinct design characteristics and internal architectures to optimize energy density, safety, and structural function, as highlighted in Figure 3. Cells metrics and specifications are reported in Table S4.

The Blade cell (Figure 3A) developed by the BYD manufacturer stands out for its unique thin and elongated form factor, resembling a blade. BYD’s patents<sup>46</sup> reveal that the cell is a thin and elongated prismatic design enclosed in 0.3-mm-thick aluminum case.<sup>23</sup> Inside, multiple layers of LFP cathodes and graphite anodes are stacked alternately and separated by polymer sheets. Tabs are positioned on opposite sides and connected to the terminals on the lid, ensuring efficient electrical contact. Safety is enhanced by a protective insulation film, side strips, and a pressure relief valve, while the rigid case also contributes to the rigidity and integrity of the pack.<sup>24</sup> The second cell, CATL BTF0 prismatic cell (Figure 3B) used by Tesla for the Model 3 battery pack, features a dual flat-wound jelly-roll structure enclosed in a 1-mm-thick aluminum case. Each jelly roll integrates current collector foils individually folded and welded to tabs located at the top of the cell. An insulating resin layer prevents short circuits, while the positive

## A BYD BLADE



## B CATL BTF0



## C BYD C49

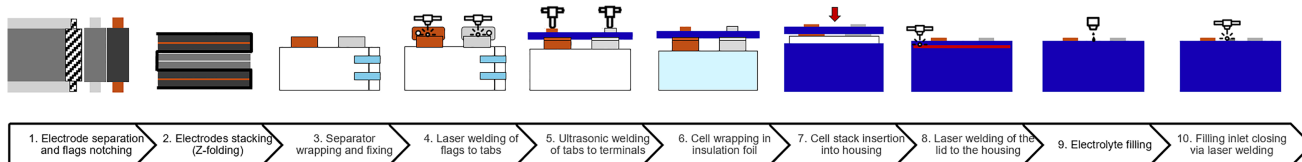


**Figure 4. Prismatic and blade cells assembly process steps**

The comparison highlights the key differences in connections and housing welding operations depending on cell geometry and electrode configuration. Each schematic step was reconstructed based on descriptions and data from published literature sources.<sup>37,40,48,50–54</sup>

- (A) BYD 138Ah blade cell.  
(B) CATL BTF0 161Ah cell.  
(C) BYD C49 100Ah cell.

and negative terminals are positioned on the cell cap.<sup>22,47</sup> The BYD C49 prismatic cell (Figure 3C), uses a conventional laminated electrode design housed in a rigid aluminum casing. Current collector foils extend from the top of the stacked layers and are connected to terminals on the cell cap. A pressure relief vent is integrated into the lid to enhance safety.<sup>48,49</sup>

The main differences in geometry, cell architecture, and components are reported in Table S5.

Figure 3 also illustrates a comparative analysis of the volumetric distribution of components in the previously described prismatic cells, for which detailed volumetric values are reported in Table S6. Volumes have been calculated from the reconstructed CAD models. As shown in the chart, the BTF0 cell by CATL reaches the highest volumetric efficiency of all cells assessed, with active materials comprising almost 80% of the total volume. The flat jelly-roll configuration creates a notable efficiency, which results in a low casing fraction of 7%, maximizing the volume dedicated to energy-storing materials. The BYD Blade cell, while adopting a prismatic stacked configuration, achieves a similar active material fraction at ~78%. This is in part due to its thin, 0.3 mm casing of aluminum. While the notable dimension of the aluminum enclosure slightly increases the inactive volume, it provides sufficient mechanical stiffness along the long, narrow design of the cell. The BYD C49 cell has an active material fraction of ~77%, which is slightly reduced compared

to the other cells, primarily due to a thicker casing, which increases inactive volume from a design perspective. This added casing, however, does provide mechanical stiffness and increased safety against external loading.

Overall, we observe a clear relationship between design and material volume or fraction: the BTF0 electrodes design effectively maximize active volume by incorporating the active materials in a space-efficient rolled design in the wound formation, while the prismatic stacked designs of the Blade and C49 use a small volumetric penalty in the inactive volume for increased rigidity.

### Prismatic cell assembly

The assembly throughput of a prismatic cell depends on the electrode's configuration, which can be produced from either a winding or stacking process. Prismatic cells are assembled by stacking multiple sheets of anode, separator, and cathode by either Z-stacking or single-sheet stacking. Alternatively, the cathode can be sandwiched by a separator, which allows for the stacker to pick up the anode and cathode and lay them on one another, which is a much faster process. The prismatic winding process resembles that of cylindrical cells but differs in the shape of the mandrel.

The assembly process steps for each prismatic cell configuration were reconstructed from literature sources<sup>37,40,48,50–54</sup> and are illustrated in Figure 4.

The assembly process of prismatic lithium-ion cells begins with the cutting and preparation of electrodes and metal foils.<sup>37,54</sup> Electrodes are stored in rolls and processed into sheets or strips matching the manufacturer's cell geometry.<sup>40</sup> For BYD Blade and BYD C49 (stacked prismatic formats), electrodes are shaped by die punching or laser notching,<sup>3</sup> while for the Tesla BTF0 (wound-electrodes format) slitting of continuous electrode rolls is employed.<sup>55</sup> In this phase, the edge integrity is critical: rough or frayed edges may promote short circuits or dendrite growth. Laser cutting offers clean edges and minimal burr formation, whereas mechanical punching requires frequent tool maintenance to maintain accuracy.<sup>56–58</sup> Coating removal near the tab area is performed by selective coating patterns or localized laser ablation.<sup>3</sup>

The BYD Blade and BYD C49 adopt stacked electrodes with Z-folded separators, while the Tesla BTF0 features a flat-wound jelly roll. In stacked cells, continuous separator foils are folded alternately with anode and cathode sheets, guided by vacuum suction and vision alignment. The separator's web tension and folding velocity are critical; excessive stress leads to foil tearing.<sup>43</sup> For both cells, an additional phase is necessary to wrap and fix the separator around the stack.<sup>23,51</sup> In wound designs, as in the BTF0, a flat mandrel defines the rectangular winding profile.<sup>22</sup> This geometry subjects the composite layer to tension and bending stresses at the winding radius, increasing internal mechanical strain.<sup>55,59</sup> The stacked configuration, in contrast, ensures uniform pressure distribution and easier thermal management but requires more precise handling and alignment.

Following electrode preparation, welding connections are performed on current-collector foils to tabs. In the BYD Blade, electrode flags are first compacted and joined ultrasonically, then laser welded to the busbar. This dual process minimizes space and ensures high electrical contact reliability. The BYD C49 employs a laser-welding operation with a simplified foil-to-tab layout that reduces welding complexity, contributing to higher throughput and reduced particle generation.<sup>54,60,61</sup> This is followed by an ultrasonic welding phase to join tabs to outer terminals.<sup>51</sup> In the Tesla BTF0, the foil-to-tabs connection is made by ultrasonic welding, while tabs are laser welded to the terminals on the cell lid.<sup>22</sup>

In BYD C49 and CATL BTF0 cell assembly process, the electrode stack/jelly roll is wrapped in insulating film and then inserted into aluminum housings. For the wound cell, the two flat jelly rolls are folded upward before the insulation phase.<sup>22,51,62</sup> In both cells, the housing closure is performed via laser welding of the lid, using pulsed or continuous beams that ensure high mechanical and hermetic quality.<sup>48,50</sup>

In the BYD Blade cell, the housing is inserted, closed by laser welding, and then each metal tab is laser welded to the outer terminals.<sup>23</sup>

Subsequent electrolyte filling and filling-port sealing complete the assembly process. A metal pin is inserted and laser welded to the lid to secure the filling hole.<sup>22,23,51</sup>

From a manufacturing perspective, the BYD Blade involves more welding operations than other prismatic formats, but its large dimensions and high energy capacity per unit enable significant economies of scale and simpler module integration. The CATL BTF0, based on a flat-wound core, achieves high volu-

metric efficiency but introduces greater mechanical strain and winding precision demands.

### Key considerations in prismatic cells

The main differences in geometry, electrode design, and production processes between the studied prismatic cells are summarized below.

- The BTF0 cell achieves the highest active-material fraction through its flat jelly-roll design.
- The thinner aluminum housing of the Blade cell lowers inactive mass.
- Stacked formats offer planar heat dissipation and higher rigidity, whereas wound designs concentrate heat centrally and require strict tension control.
- Stacked cells involve more cutting, welding, and alignment steps; wound cells enable faster continuous manufacturing with fewer joints.

### Pouch cell

Large pouch cells combine high energy density, low weight, and flexible geometry, making them suitable for automotive and heavy-duty applications.<sup>18</sup> They consist of stacked electrodes sealed in foil pouches, providing efficient space use but limited mechanical stability and susceptibility to swelling. At battery-pack level, external support structures are required, and terminal placement influences the output (opposite sides for power, same side for energy). Despite their versatility and capacity range, safety integration and venting control remain major challenges.<sup>10,12,26</sup>

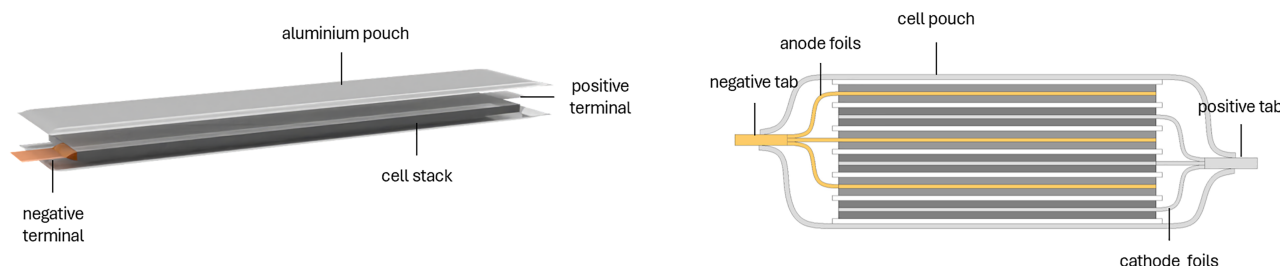
### Pouch cell design and components

The pouch cell chosen for this study (see Figure 5) is a large-format pouch cell with a nominal capacity of 78 Ah produced by LG Chem and used in the Volkswagen ID Family car's battery pack. Metrics and specifications of the cell are reported in Table S7. Measured geometry data and internal structure layout are taken from the teardown provided by Günter et al.<sup>19</sup>

The cell stack, composed of alternating anode, cathode, and separator layers, is inserted into a deep-drawn aluminum pouch sealed with multilayer polymer tapes to ensure mechanical protection and gas tightness.<sup>19</sup> The sequence of electrodes follows a repeating separator-anode-separator-cathode pattern, ending with an anode on one side and a separator on the opposite side, ensuring electrical insulation and balanced compression during operation.<sup>19</sup>

The anode consists of a graphite-based coating on copper foil, while the cathode uses an NMC-type chemistry (NMC 712) designed to balance energy density, thermal stability, and cycle life. This intermediate composition between NMC622 and NMC811 combines the higher energy density of the latter with the improved stability of the former, making it suitable for automotive applications.<sup>63</sup> Each electrode includes a metallic current collector and an active layer on both sides, optimized for uniform ion transport and mechanical strength. The separator is a thin polymer film that provides electrical insulation and ionic conductivity between the electrodes.<sup>19</sup> Current collector tabs made of aluminum (positive) and nickel-plated copper (negative) are placed at opposite ends of the long electrode edges to reduce

## A Components layout and cross section



## B Volume distribution

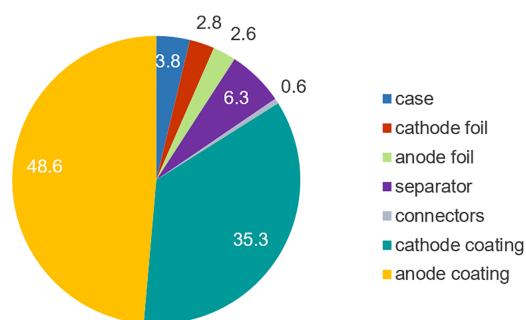


**Figure 5. Component layout and internal volume distribution in LG Chem E78 pouch cell**

Exploded 3D reconstruction shows the main components of the pouch cell, including pouch, electrode-separator layers and tabs. The pie charts below quantify the internal volume allocation among active and inactive components.

(A) Cell architecture and simplified cross section.

(B) Component volume distribution.

electrical resistance and improve heat dissipation.<sup>19,25</sup> The pouch casing, made of laminated aluminum foil, ensures a lightweight structure but relies on external compression and housing support for mechanical stability. Unlike prismatic cells, pouch formats do not include a venting valve: internal pressure is instead released through a controlled deformation zone, designed to bulge or rupture safely under excessive pressure.<sup>19,64</sup> This pressure-relief mechanism, integrated directly in the pouch material, improves safety while maintaining compactness and low mass. Cell swelling is then managed at system level in the battery pack.

All geometric parameters and dimensions are summarized in Table S8.

The volumetric distribution of components within the pouch cell is illustrated in Figure 5B, highlighting the predominance of active materials. Relative values are reported in Table S9. The combined anode and cathode coatings occupy over three-quarters of the total cell volume, confirming the design's focus on energy efficiency. Non-active elements represent only a small fraction of the overall volume. In particular, the connector volume fraction is exceedingly small because the pouch design lacks the rigid terminal assemblies typically used in prismatic cells. The thin aluminum pouch minimizes structural component mass while maintaining protection and sealing, allowing most of the internal space to be devoted to energy-storing materials. This configuration results in high volu-

metric utilization and superior energy density compared with other cell formats.

### Pouch cell assembly

Pouch cells differ from cylindrical and other prismatic cells by containing tabs welded to the outside of the cell that allow for electronic transport, so all edges of the pouch must be hermetically sealed to avoid reactions between water and the liquid electrolyte and/or the cathode. Unlike other cell formats, pouch cells also require stack pressure to improve cycle life because their soft casings do not provide stack pressure. The lightweight and the absence of a hard case and safety makes pouch cells also prone to swelling.<sup>65</sup> Figure 6 summarizes the key stages of the assembly process for a commercial pouch cell, available in literature.<sup>19,25,40,51,58,60,66,67</sup>

As for prismatic cells, the process begins with electrode separation and flag notching, where anode, cathode, and separator sheets are cut from roll materials using precision laser cutting to ensure clean edges and minimize burrs.<sup>19,58</sup> The separated sheets are then combined through Z-folded stacking in the sequence separator-anode-separator-cathode, ending with a separator layer. Adhesive tape is used to fix the stack before pouch insertion.<sup>40,53,66</sup> The stack can be laminated afterward by applying elevated temperature and pressure to secure the position of the sheets.<sup>19,40</sup> Conductor tabs made of aluminum and nickel-plated copper are welded to flags. From the teardown images,<sup>19</sup> the tabs display different patterns embossed on the front

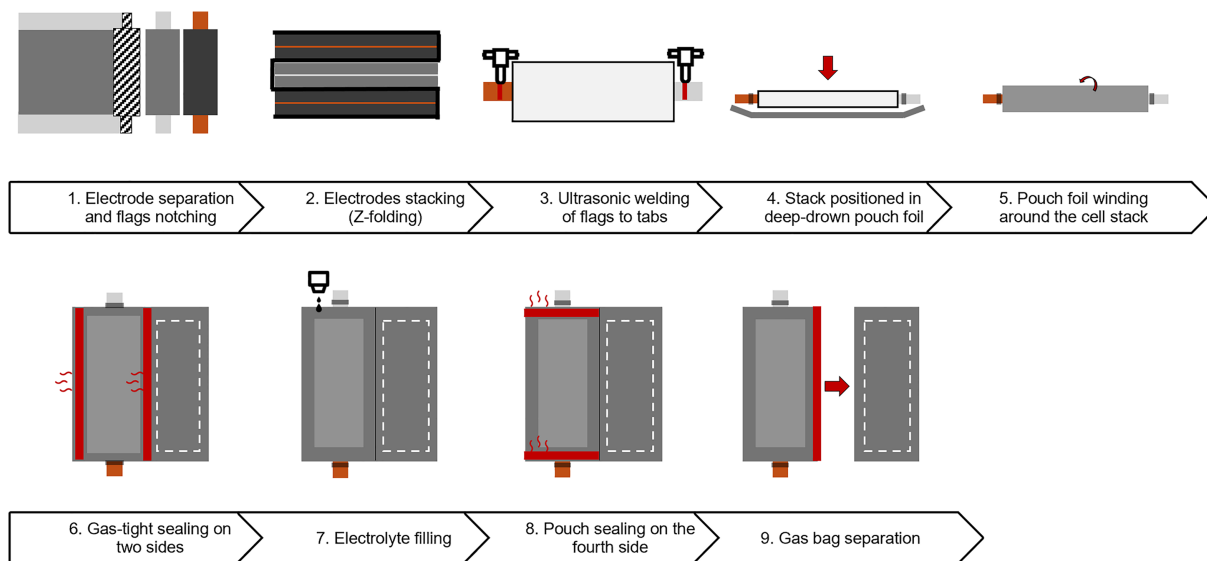


**Figure 6. Cell assembly process steps for LG Chem E78 pouch cell**

Each schematic step was reconstructed based on descriptions and data from published literature sources.<sup>19,25,40,51,58,60,66,67</sup>

side compared to the back side. These patterns are created through ultrasonic welding in the metal.<sup>40,44</sup> The stacked electrodes are then inserted into a deep-drawn aluminum-polymer pouch, which is subsequently wrapped around the cell stack.<sup>40,51</sup> Using plastic-metal laminate for the cell pouch reduces the amount of material needed for cell packaging.<sup>67</sup> The pouch foil is sealed gas-tight on two sides using impulse or contact heat sealing, leaving tab sides open for electrolyte injection.<sup>40,51</sup> The next phase is electrolyte filling under vacuum, during which repeated evacuation-filling cycles promote full wetting of the electrodes. Once filling is complete, the remaining side of the pouch is sealed.<sup>19</sup> According to literature,<sup>68</sup> gases generated during cycling are released through a degassing step, where the gas pocket is pierced, the trapped gas is evacuated under vacuum, and the opened side is resealed close to the stack. The external gas bag is then removed, and the cell is sealed into its final form. This step improves dimensional stability and volumetric energy density.<sup>54,68,69</sup>

#### Key considerations in pouch cell

The main design and process features of pouch cells are summarized below:

- lightweight terminals and housing with an integrated pressure-relief mechanism maximizing active volume and reduces inactive mass,
- high energy density enabled by compact architecture and NMC-based cathode chemistry, and
- limited mechanical strength of the flexible casing requiring external structural support within the battery pack.

#### Cells energy metrics and design trade-offs

Results from CAD models, teardown, patents, and datasheets available have been collected in Figure 7 to compare the key design parameters, properties, and assembly processes of all cells examined in this study. This approach enables a detailed

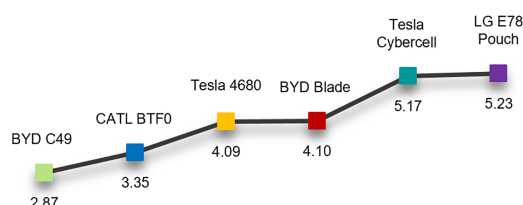
assessment of the trade-offs between cells energy and design choices.

Figure 7A shows higher active-to-inactive ratios for the cylindrical Cybercell and LG pouch cell ( $>5$ ) and lower values ( $\leq 4$ ) for other formats (a more comprehensive comparison of component volume usage is reported in Figure S1). Cylindrical cells achieve efficient space use through wound electrode design, and the new-generation 4680 format further improves this via optimized internal architecture and reduced inactive component mass. The pouch cell also shows superior volumetric efficiency due to a lightweight casing, allowing more internal volume for electrodes but with lower mechanical strength. In contrast, prismatic cells exhibit lower active fractions because of thicker housings and heavier contact components that enhance rigidity and safety. Also, the choice of cathode chemistry significantly impacts cell energy, particularly in terms of nominal energy and energy density (see Figure 7B). Prismatic and blade cells using LFP cathodes deliver high nominal energy (up to 515 Wh for CATL BTF0 flat-wound prismatic) but relatively low energy density (160 Wh/kg and 420 Wh/L in the BYD Blade) because of the lower theoretical capacity of cathode material ( $\sim 170$  mAh/g for LFP<sup>70</sup> vs.  $\sim 250$  mAh/g for NMC811<sup>71</sup>). Their larger size compensates for the limited intrinsic energy density of LFP, while ensuring excellent safety and thermal stability due to the strong P–O bonds that prevent oxygen release under stress. In contrast, NMC-based cylindrical and pouch cells achieve much higher volumetric and specific energy density (over 600 Wh/L and 272 Wh/kg in Cybercell), enabling compact and lightweight designs suited for high-performance vehicle applications. However, this advantage comes with trade-offs in safety and cycle life, since NMC cathodes are more reactive and prone to degradation mechanisms such as cation mixing, transition-metal dissolution, and cathode-electrolyte interface instability during cycling.<sup>72</sup>

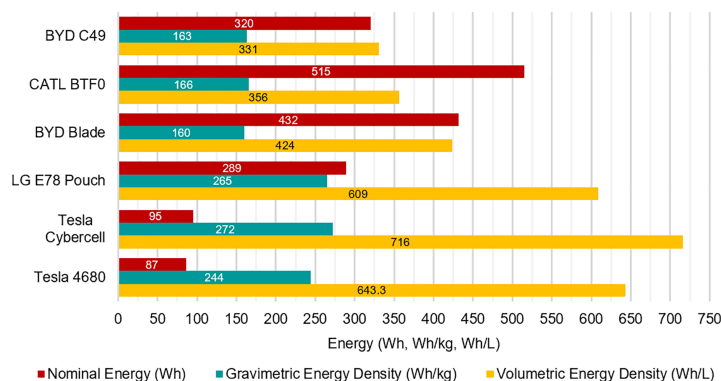
The manufacturing complexity of different cell formats is compared in Figures 7C and 7D, based on the number of cutting



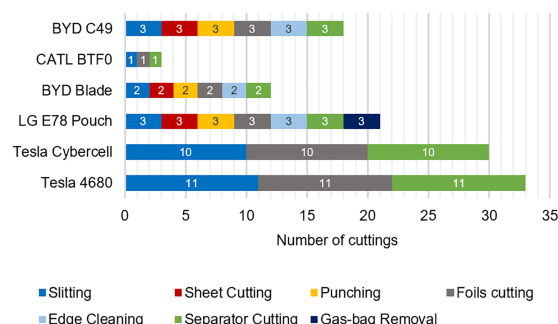
## A Active/inactive volume ratio



## B Nominal Energy and Energy Densities



## C Cutting operations



## D Welding operations

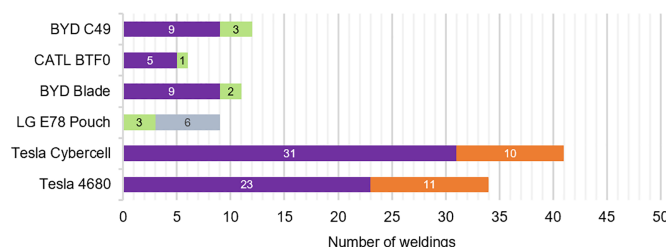


**Figure 7. Design, energy metrics, and manufacturing characteristics of battery cells**

(A) Active-to-inactive volume ratio ( $V_a/V_d$ ), calculated from CAD-based cell reconstruction. Here,  $V_a$  includes the electrochemical stack volume (electrodes), while  $V_d$  includes non-electrochemical volumes (e.g., casing/can, tabs, current collectors, and other structural elements), as defined in the methods.

(B) Nominal energy ( $E_{nom}$  (Wh)), gravimetric energy density ( $E_{nom}/m_{cell}$ ,  $Wh\ kg^{-1}$ ), and volumetric energy density ( $E_{nom}/V_{cell}$ ,  $Wh\ L^{-1}$ ) for each format, using cell mass  $m_{cell}$  and external cell envelope volume  $V_{cell}$ . Differences in cell chemistry are highlighted: prismatic BYD C49, blade, and CATL BTF0 with LFP cathode, LG E78 pouch cell with NMC712, cylindrical Tesla 4680 with NMC811, and Tesla Cybercell with NMC955.

(C) Number of cutting operations per kWh, computed as  $(N_{cut}/E_{nom}) \times 1000$ .

(D) Number of welding operations per kWh, computed as  $(N_{weld}/E_{nom}) \times 1000$ . Operation counts are reported as integers and obtained by counting only full cells per kWh (i.e., partial cells are excluded).

All values are derived point estimates based on nominal specifications and CAD-based reconstruction assumptions.

and welding operations per kWh, which are interpreted here as distinct process stations rather than the total number of repetitive mechanical cuts or welds to reflect industrial scalability in a gigafactory setting (where each operation corresponds to a dedicated workstation). Cylindrical cells (4680 and Cybercell) show the highest process count, due to their roll-to-roll workflow that includes slitting, edge trimming, and jelly-roll cutting, followed by laser and spot welding for tab and terminal joining. Although the cutting sequence is efficient and automated, the number of welding phases increases overall process intensity. In contrast, stacked prismatic cells (BYD C49 and Blade) involve more types of cutting operations, such as sheet cutting, notching, separator trimming, and edge cleaning, since each electrode layer must be shaped individually. The Blade adds two assembly steps compared with the cylindrical cell, integrating ultrasonic pre-welding and laser busbar welding. From an industrial stand-

point, the CATL BTF0 represents a production compromise between prismatic formats, combining the simplicity of cylindrical winding with part of the electrical contact complexity of stacked cells. The pouch cell shows the lowest number of joining operations, and cutting complexity is moderate but slightly higher than prismatic formats.

From the analysis, two main strategies emerge to reduce the share of inactive components in a cell. Both aim to maximize stored energy per mass but act on different design levels. The first optimizes internal architecture while keeping the same form factor, as in the cylindrical 4680 cell. By thinning can walls, integrating current collectors, or merging sealing parts, inactive volume decreases without changing outer dimensions, improving gravimetric energy density, and simplifying assembly. The second increases active material without major production changes, as in the blade cell. Extending electrode length raises

**Table 1. Main cell-specific results and trade-offs among design, manufacturing, and process**

Cell Type	Active Volume	Assembly Pros	Assembly Cons
4680 Gen 1	80.4%	high automation and scalability	numerous and different welding operations
Cybercell	83.8%	simplified current collector welding	complex joining; precise alignment needed
LG Pouch	83.9%	few joining operations	mechanically fragile; sealing sensitivity
BYD Blade	77.0%	larger sheets, same cutting operations	larger sheets reduce handling
CATL BTF0	80.5%	hybrid process balances manufacturing intensity	additional welding vs. pure winding process
BYD C49	74.1%	mature prismatic stacking; robust mechanical integrity	many cutting operations per electrode layer

cell capacity and energy per kilogram while maintaining the same manufacturing footprint. At battery-pack level, it also reduces the number of structural components needed, thereby simplifying assembly and lowering the likelihood of pack failure due to the malfunction of an individual cell.

However, larger cells dissipate heat less efficiently from their core to the surface, heightening the risk of internal hot spots and requiring more robust thermal management. To mitigate this, large-format cells often adopt cathode chemistries with greater thermal and cycling stability, such as LFP, which provide a wider operating window and longer cycle life, despite lower energy density than NMC cathodes.

To provide a concise overview of the comparative findings discussed above, Table 1 summarizes the main assembly and design-related characteristics of the chosen cell formats shown in Figure 7 above.

### Battery pack module layout

A standard battery system in electric vehicles consists of cells assembled into modules and integrated with housing, cooling, battery management system (BMS), and electrical components. Modules contain several cells connected in a series for the total voltage and in parallel to increase the capacity, within a mechanical frame.<sup>73</sup> Multiple modules are then interconnected, along with sensors and control systems such as the BMS and thermal management, to form the full pack. The final structure is enclosed in a protective housing designed for the specific vehicle.<sup>52</sup>

To evaluate the system-level implications of the investigated cell formats, six commercial battery packs employing the corresponding cell types were analyzed and reconstructed as in Figure 8: Tesla Model Y (4680 cell), Tesla Cybertruck (Cybercell), Volkswagen ID.3 (LG E78 pouch), BYD Atto 3 (BYD Blade), Tesla Model 3 (CATL BTF0), and Mercedes CLA 200 (BYD C49). The selected systems represent distinct design architectures and integration strategies. This assessment enables a comparative analysis of how different cell formats influence structural integration, space utilization, and energy availability within comparable packaging constraints.

#### Tesla Model Y

The Tesla Model Y battery pack (Figure 8A) consists of four modules of Gen 1 4680 cylindrical cells, for a total capacity of 71.5 kWh, arranged in a 92s9p configuration. The overall mass of the pack is 445 kg, including 294 kg of cells, resulting in a cell-to-pack mass ratio of 66%. Each module integrates 107 cells configured 23s9p.<sup>74</sup> The electrical interconnection relies

on aluminum busbars with single-sided plating only on the welded surface. Busbars are narrower in parallel connections and wider in series sections, and the relaxation of flatness tolerances further simplifies production by eliminating rework and inspection steps previously required by welding constraints.<sup>75</sup> Thermal management is achieved through north-south oriented serpentine cooling plates circulating a water-glycol mixture. Each module contains three cooling channels that cool the edges of two adjacent rows of cells, with a contra-flow inlet-outlet arrangement minimizing temperature gradients along the pack length. The cells are bonded to extruded cooling lines using a thermally conductive adhesive in a so-called bandelier assembly. The pack functions as a structural element within the vehicle's chassis: it features a stamped steel tub without internal extrusions, incorporating transverse beams for seat mounting but not directly tied to the side sills. Cells are housed in polycarbonate trays adhered to the base plate with mica adhesive and vent downward through a mica layer. Fiberglass phenolic barriers are placed between modules to limit thermal propagation in the event of runaway. A polyurethane-based structural foam is injected after busbar installation to fill internal voids and secure the assembly, while the steel lid (laser welded along the perimeter and thickened in the front and seat-mount regions) ensures rigidity and impact resistance. A deliberate air gap is maintained beneath the cells since no epoxy bonding connects them to the chassis. Along both longitudinal sides, high-durometer polyurethane foam inserts create compliant crush zones that absorb side-impact energy, protecting the cells by deforming without excessive compression. The entire assembly is secured using only 16 fasteners, enabling simplified assembly and serviceability while maintaining structural integrity and lightweight design.<sup>74–76</sup>

#### Tesla Cybertruck

The Cybertruck produced by Tesla employs the second-generation 4680 cells (Cybercell) and functions as a structural element of the vehicle chassis (Figure 8B). Seats are mounted directly onto the pack, eliminating additional body layers and simplifying assembly. The pack configuration is 192s7p (1,344 cells total), providing 123 kWh of usable energy.<sup>77</sup> The total pack mass is 721 kg, including 470.5 kg of cells, resulting in a 65% cell-to-pack ratio. The overall structure and layout are similar to the Model Y battery pack, but it differs in cell and structural component arrangement. The structure features a bottom metal cover sealed with room-temperature-vulcanizing (RTV) adhesive and a single-layer cell layout arranged north-south. The negative

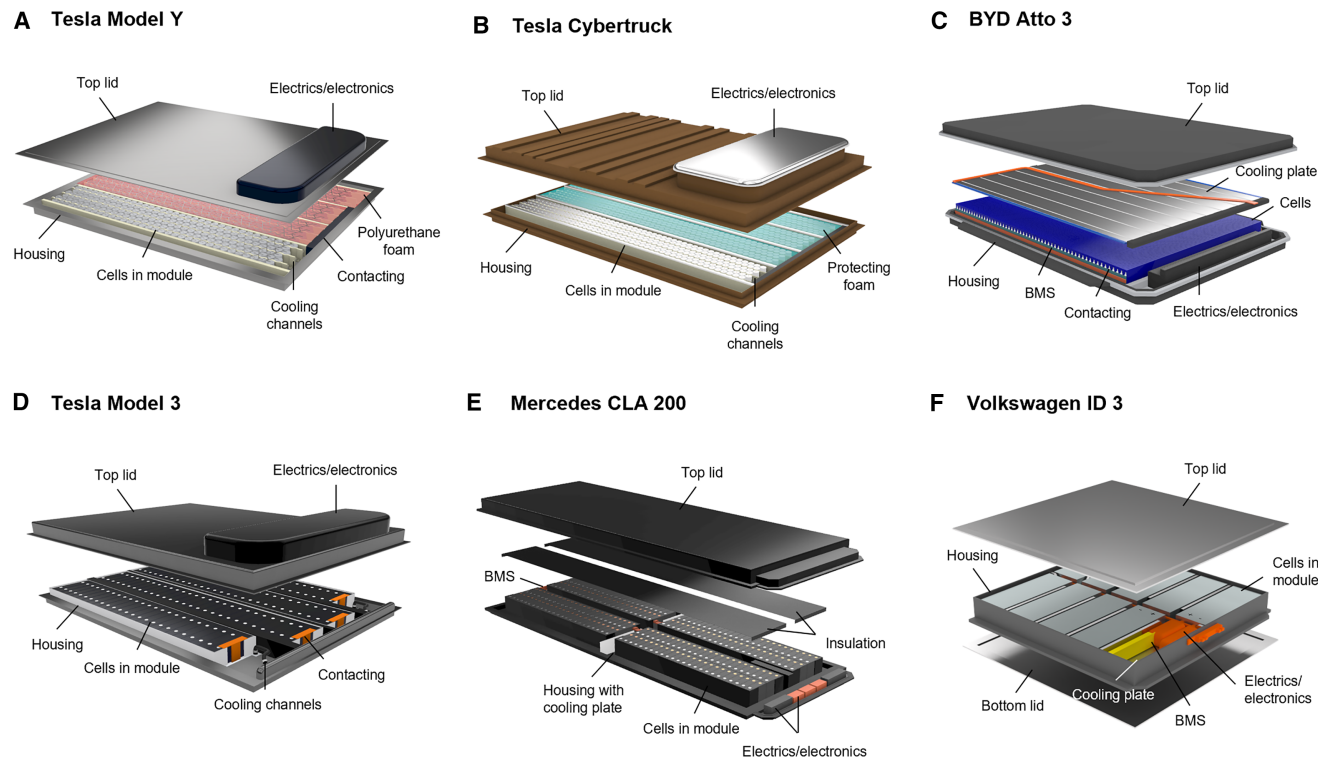


**Figure 8. Battery pack architecture**

The comparison highlights different cell-to-pack layouts and cooling strategies across the selected commercial electric vehicles. Each figure shows the arrangement of cells, cooling channels, electronics, and structural components, based on literature and teardown data.<sup>29,74–92</sup>

- (A) Tesla Model Y with 4680 cells.
- (B) Tesla Cybertruck with 4680 Gen 2 cells.
- (C) BYD Atto 3 with Blade cells.
- (D) Tesla Model 3 with CATL BTF0 cells.
- (E) Mercedes CLA 200 with BYD C49 cells.
- (F) Volkswagen ID.3 with LG Chem E78 cells.

side of the battery pack is on the bottom, and the positive terminals of the cells are on the other side of it, which has connections to the battery management system. The lid rests on vertical standoffs. Plastic trays are omitted, with void spaces used for structural function and gas venting. The pack incorporates integrated crumple zones and an external BMS unit positioned at the front. Thermal management relies on serpentine coolant plates circulating a water-glycol mixture, identical to those in the Model Y. Safety features include green foam and mica barriers for thermal runaway mitigation, venting channels for gas expansion beneath the cells, and pressure-equalization membranes with spark arrestors.<sup>77–79,93</sup> A patented self-activated drain system<sup>94</sup> allows automatic discharge of leaked coolant, preventing electrical shorting. Based on Tesla patent WO2021102340A1,<sup>93</sup> the lower structure serves as a mechanical and energy-absorbing element, combining stiffness for normal operation with controlled deformation under impact. This design enhances crashworthiness, thermal safety, and mechanical integration while minimizing mass and improving manufacturability.

#### BYD Atto 3

The BYD Atto 3 uses long prismatic 135 Ah Blade cells (Figure 8C). The pack connects roughly 100–120 cells in a series

in a cell-to-body layout without separate modules.<sup>95</sup> The battery pack output energy is 51.8 kWh and the mass 420 kg,<sup>96</sup> reaching a 77% cell-to-pack ratio with 324 kg of cells. The cells are bonded directly to the aluminum tray, enhancing structural stiffness but limiting ease of replacement. Electrical connections alternate polarity along the pack width, while small circuit boards serve as fusible links between busbars.<sup>80,81</sup> The BMS and control electronics are positioned at the front within the structural tunnel section of the vehicle.<sup>82</sup> Cooling is provided by a single large aluminum plate fixed above the cells, featuring front-side inlet and outlet ports. This design minimizes joints and potential leaks, while the cooling plate itself adds another safety barrier between the cells and passenger compartment. However, uniform coolant distribution depends on strict flatness and assembly precision. The pack exterior incorporates rubber bumpers and a thin composite lid.<sup>82,83,95</sup> The dense cell packing, combined with LFP's high thermal stability, ensures excellent safety in case of mechanical deformation or thermal stress.

#### Tesla Model 3

The Tesla Model 3 equipped with CATL's LFP pack (Figure 8D) uses BTF0 prismatic cells. The battery is organized into four modules (two outer 25s1p and two inner 28s1p) for a total

configuration of 106s1p. The total pack mass is 438 kg, of which 328.6 kg are cells, yielding a cell-to-pack ratio of 74%.<sup>84</sup> The modules are arranged longitudinally, with the prismatic cells directly attached and compressed inside the structural tray. This configuration turns the pack into a semi-structural component that contributes to overall body stiffness.<sup>84–86</sup> The electrical interconnections rely on laminated flex circuits integrating voltage and temperature sensing. Laser-welded busbars ensure precise and consistent connections, reducing both electrical resistance and manufacturing tolerance requirements. The BMS and circuit boards are housed in a front-mounted enclosure designed for vertical assembly and simple serviceability.<sup>84,86</sup> Thermal management is handled by a liquid cooling system using ethylene glycol flowing beneath the cells through aluminum plates. The cooling loop connects to the vehicle's HVAC chiller, enabling both heating and cooling through refrigerant exchange.<sup>84,85,87</sup> Structurally, the pack is sealed by a metal lid to ensure waterproofing and mechanical integrity. Air gaps above and below the modules protect against debris intrusion and allow limited deformation under impact.<sup>86</sup>

#### **Mercedes CLA 200 (2025)**

The 2025 Mercedes CLA 200 (Figure 8E) adopts BYD C49 LFP prismatic cells divided into 4 modules of 48 cells in series (192 cells in total), providing a battery of 61.4 kWh.<sup>97</sup> The pack weighs 484 kg and achieves a 75% cell-to-pack mass ratio. It combines a steel outer frame with an aluminum tray and die-cast internal reinforcements. Both modules and cooling plates are bonded to the base frame using structural adhesive, simplifying assembly and improving stiffness. The BMS incorporates reversible and irreversible high-voltage disconnection mechanisms, including pyrotechnic switches. These allow controlled isolation of the HV system during faults or impacts, preserving occupant safety and vehicle integrity. The cooling system is integrated into the base frame, with all fluid joints located externally to isolate high-voltage zones.<sup>88</sup> Although this approach slightly limits thermal efficiency, it significantly enhances safety and serviceability. Mechanically, the pack undergoes “touch-down management” tests, in which high loads simulate curb strikes to verify underbody protection. The modular layout minimizes busbar length and interconnections, contributing to a robust and repairable design.

#### **Volkswagen ID.3**

Volkswagen's ID series vehicles are built on the Modular Electric Drive Matrix (MEB) platform (Figure 8F), which integrates the battery pack within the vehicle floor to achieve optimal weight distribution.<sup>89</sup> The ID.3 employs LG Chem E78 pouch cells based on NCM cathode chemistry,<sup>90</sup> arranged in 9 modules (each configured as 12s2p) for a total of 216 cells,<sup>91</sup> resulting in a total pack output of 61 kWh. The pack has a total volume of 288 L and an estimated mass of 376.7 kg, yielding a cell-to-pack mass ratio of 64.5%.<sup>92</sup> The battery pack mass was estimated based on the available data for the Volkswagen ID.4 battery system,<sup>89</sup> considering the modular architecture. BMS and relays are located in the auxiliary slot on the right side. Rear busbars interconnect the modules, while voltage and temperature monitoring occur at the module level.<sup>89,91</sup> Thermal management is achieved through conduction: heat paste is applied beneath each module to transfer heat to the aluminum baseplate, while a cooling circuit

runs along the rear side of the pack. The coolant enters and exits on the left side, flowing through parallel channels with small restrictions to balance flow distribution. No coolant is present inside the modules or between the cells, which simplifies assembly and eliminates the risk of internal leakage.<sup>98</sup> Structurally, the pack employs high-grade aluminum housing that includes a protective back sheet and internal reinforcement bars. A 15 mm air gap between the protective plate and the coolant plate provides both deformation tolerance and impact absorption. The design balances mechanical protection, modularity, and thermal management at moderate cost.<sup>89,90</sup>

#### **Key considerations in battery-pack configurations**

Table 2 summarizes the main specifications of the analyzed battery packs, highlighting differences in cell format, structural integration, and cooling strategy, to provide a direct comparison of energy output, mass distribution, and cell-to-pack efficiency. Additional metrics of the analyzed battery packs are reported in Table S10.

#### **Energy and packaging evaluation of battery packs**

The demand for longer battery life in electric vehicles continues to grow, but battery packs still face challenges with low space utilization.<sup>46</sup> The impact of efficient packaging is particularly significant in achieving greater driving ranges, as it allows for more space to accommodate additional cells. Moreover, utilizing the available space efficiently offers additional benefits: reduced space requirements lead to less material used for the housing and other components, resulting in a lighter battery system. This, in turn, further enhances the vehicle's range and can also enable the downsizing of other components, as their strength requirements decrease due to the battery system's more compact and lightweight design.<sup>99</sup>

Data in Figure 9 reflect the performance and structural characteristics highlighting the main key metrics, such as energy density, gravimetric cell-to-pack (GCTP) ratio, mass, voltage, capacity, and total energy. The volumetric energy density is calculated using the estimated battery-pack volume derived from the available teardown data. This multi-parameter comparison provides insights into how cell format influences overall pack efficiency and design trade-offs in electric vehicle applications.

The comparison among the three charts in Figures 9A–9C reveals that the relationship between energy density and cell arrangement through the GCTP is strongly mediated by cell chemistry. Prismatic cell-based battery packs (CLA 200, Model 3 LFP) exhibit lower gravimetric and volumetric energy densities, consistent with the intrinsic limitations of the iron-phosphate chemistry. However, these same LFP packs achieve the highest GCTP values (around 74%–75%). This indicates that their lower heat generation and simpler mechanical requirements allow a more efficient use of internal pack volume. The BYD Atto 3 (using the blade cell), instead, achieves one of the highest volumetric energy densities within the LFP group while maintaining a top-tier GCTP, reflecting the spatial efficiency of the Blade architecture. In contrast, the NMC-based packs (Tesla 4680, Cybercell, and LG pouch) attain higher energy densities, with the Cybertruck cell achieving the upper end of both gravimetric and volumetric scales. Despite this, they display markedly lower GCTP



**Table 2. Battery pack specifications and layout**

Vehicle	Cell Format	Configuration	Energy (kWh)	Pack Mass (kg)	Cells Mass (kg) <sup>a</sup>	GCTP Ratio (%) <sup>a</sup>	Structural Integration	Cooling System
Tesla Model Y	4680 Tesla cylindrical NMC	92s9p (4 modules) = 828 cells	71.5	445	294	66	structural battery pack	serpentine glycol cooling + drain system
Tesla Cybertruck	4680 2 Tesla cylindrical NMC	192s7p (4 modules) = 1,344 cells	123	721	470.5	65	load-bearing structural pack	serpentine glycol + drain system
BYD Atto 3	BYD Blade prismatic LFP	≈100–120 in series (no module)	60.5	420	317	75	cell-to-body layout	single top plate cooling
Tesla Model 3	CATL BTF0 prismatic LFP	106s1p (4 modules)	55	438	328.6	74	semi-structural assembly	liquid glycol under-cell plate
Mercedes CLA 200	BYD C49 prismatic LFP	48s1p (4 modules) = 192 cells	58	484	365*	75	non-structural steel-Al frame	base-integrated liquid cooling
VW ID.3	LG Chem E78 pouch NMC	12s2p (9 modules) = 216 cells	61	376.7	231.8	64.5	non-structural aluminum tray	rear cooling plate with parallel flow

Data are taken from literature and teardown ref. <sup>29,74–92,94–98</sup>.

<sup>a</sup>Calculated data.

values, between 64% and 66%. This divergence can be attributed to the geometry of cylindrical cells and more demanding structural and thermal management requirements of NMC chemistries, which increase the proportion of non-active materials within the pack.

Figure 9D illustrates the correlation of nominal energy delivered by the studied battery packs with nominal capacity and voltage. In blade- and prismatic-based battery packs, cells are all connected in series to achieve the required voltage for vehicle operation, so the total capacity of the battery pack matches the capacity of a single cell. In contrast, to achieve an adequate nominal capacity in the battery pack, the cylindrical and pouch cells need to be connected also in parallel, because of significantly lower individual capacities. Configurations with all cells in series maximize energy by combining high voltage with moderate parallelization but at the cost of greater BMS complexity and stricter safety requirements. While series-connected cells charge and discharge simultaneously at the same rate, minor voltage imbalances inevitably arise due to factors such as manufacturing variations, aging, thermal conditions, self-discharge rates, internal impedance differences, and uneven charging or discharging. These imbalances can result in overcharging or deep discharging of certain cells, potentially leading to distortion and affecting the overall performance, safety, and operation of the battery pack. Furthermore, if a single cell fails, the entire series ceases to function due to the interruption of current flow.<sup>100</sup>

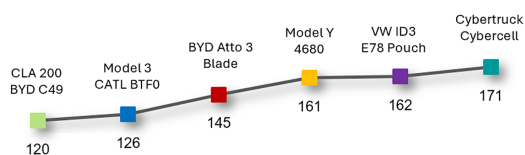
The radar plot in Figure 9E provides a consolidated view of the seven performance dimensions and reveals a set of clearly differentiated engineering signatures, each shaped by the interplay among chemistry, structural integration, and pack-level design choices. The LFP-based packs exhibit strong expansion along the cell-to-pack ratio axis and comparatively compact profiles on the gravimetric and volumetric energy-density axes, reflecting structurally efficient but lower-specific-energy chemistries. Conversely, the NMC-based systems show pronounced outward extension in both energy-density metrics and a systematic retraction in integration efficiency, indicating that their higher intrinsic cell performance is counterbalanced by increased thermal and structural overhead at pack level. This contrast highlights the distinct optimization strategies that characterize each architecture and the multidimensional nature of battery-pack performance.

### Forecasted cost analysis

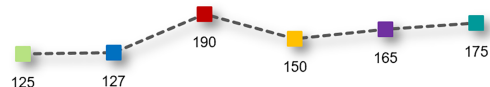
To further support the analysis of design choices, a prospective cost assessment was conducted on the six previously analyzed commercial cell formats, since battery cost has become a central metric in the design and industrialization of battery systems, still accounting for over 30% of the total vehicle cost.<sup>101</sup> In particular, the comprehensive techno-economic analysis presented by Orangi et al.<sup>102</sup> offers a detailed bottom-up model of lithium-ion cell and pack production costs, forecasting trends based on cell chemistry, manufacturing advancements, and integration approaches. Recent projections forecast continued cost declines, with cell-level costs dropping to \$20–\$30/kWh by 2030.<sup>102,103</sup> High-nickel NMC cells remain more expensive per kWh than LFP-based cells due to costly raw materials, even though they offer superior energy density.



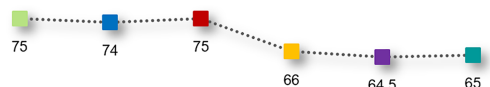
### A Gravimetric energy density (Wh/kg)



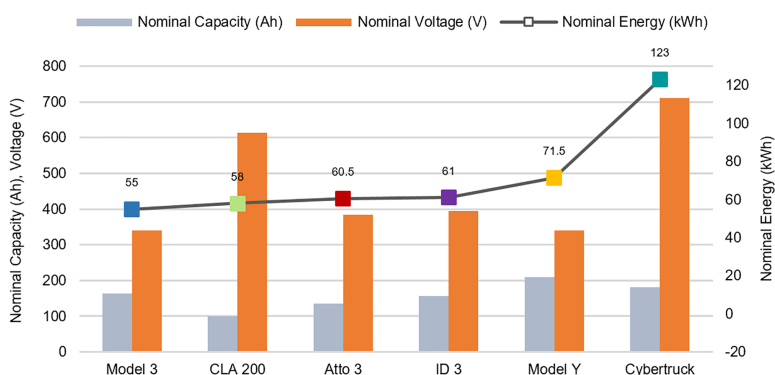
### B Volumetric energy density (Wh/L)



### C GCTP (%)



### D Voltage, Capacity and Energy



### E Battery packs main characteristics

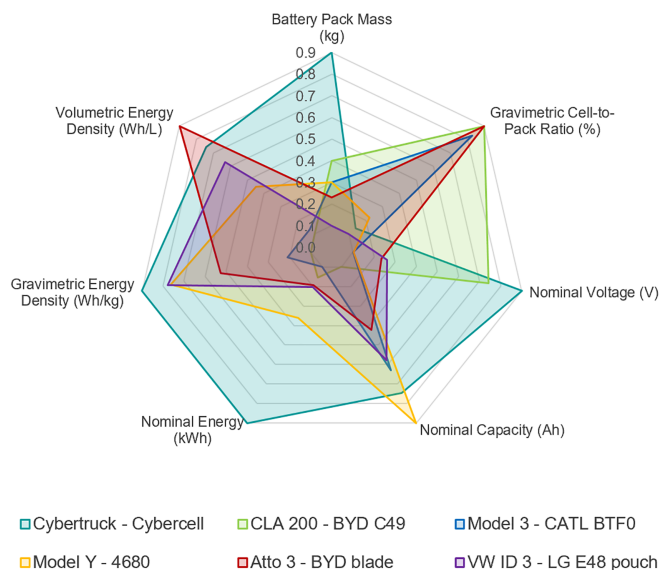


**Figure 9. Battery pack-level metrics for the six EVs considered**

(A) Gravimetric energy density ( $E_{\text{nom, pack}}/m_{\text{pack}}$ ,  $\text{Wh kg}^{-1}$ ).

(B) Volumetric energy density ( $E_{\text{nom, pack}}/V_{\text{pack}}$ ,  $\text{Wh L}^{-1}$ ).

(C) Gravimetric cell-to-pack ratio (%), calculated as  $(E_{\text{pack}}/m_{\text{pack}})/(E_{\text{cell}}/m_{\text{cell}}) \times 100$ .

(D) Pack nominal voltage (V), nominal capacity (Ah), and nominal energy (kWh), determined from series/parallel cell configurations.

(E) Radar chart summarizing the main metrics used for comparison across the battery packs.

Corresponding data are reported in [Table 2](#) and [Table S10](#).

All values are derived point estimates based on nominal specifications and pack configuration.

**Figure 10** presents a prospective cost breakdown for cell formats per kWh and the resulting battery packs, based on projections through 2030 from Orangi et al.<sup>102</sup>

The analysis clearly shows that, at cell level (**Figure 10A**), NMC-based cells remain consistently more expensive than LFP cells across the entire period considered. This cost gap is primarily driven by the intrinsic price of raw materials: the reliance on nickel and cobalt imposes a structurally higher and less flexible material cost for NMC chemistries, whereas LFP cathodes use cheaper and more stable precursors. In contrast,

LFP cells exhibit higher production costs due to processing requirements, yet this contribution is proportionally less dominant than the material component in NMC systems. Projected trends to 2030 indicate a steeper cost reduction for LFP cells. This reflects cost-learning dynamics in which an initial material-cost advantage accelerates industrial scaling, process optimisation, and technology consolidation. The low and stable cost of LFP cathode materials has enabled rapid expansion of integrated formats such as Blade and cell-to-pack, enhancing manufacturing efficiency and deepening cost declines. In contrast, NMC

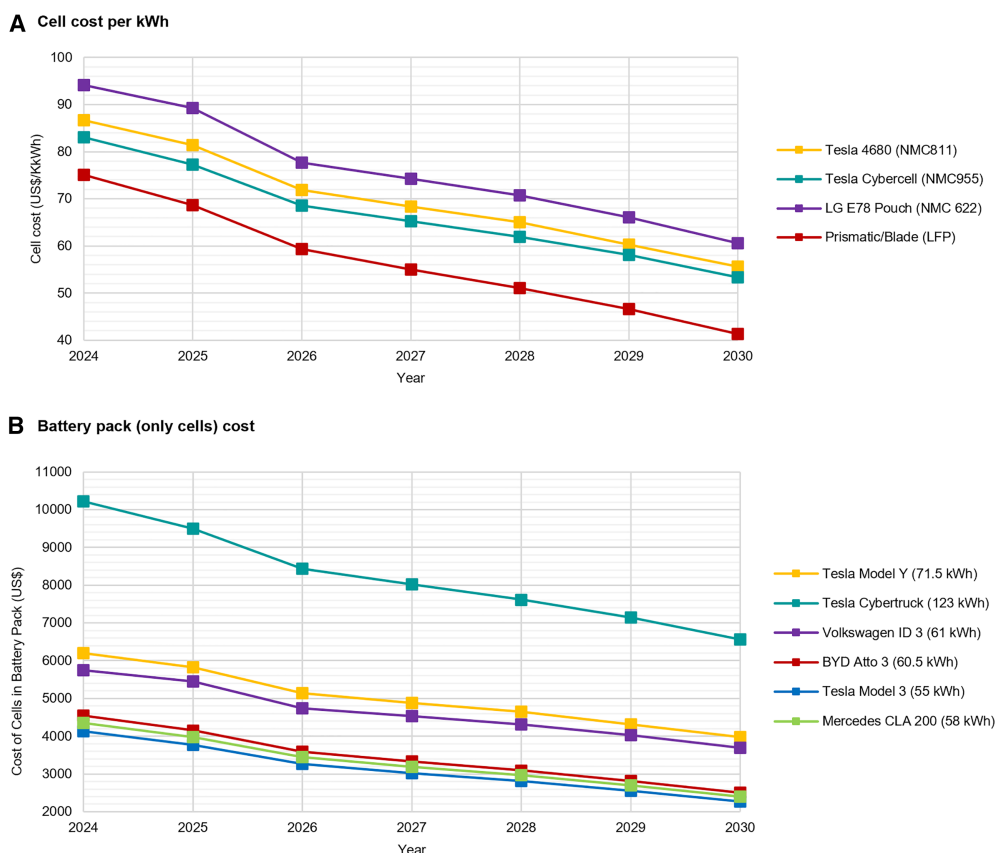


**Figure 10. Projected cell and battery pack cell-only costs (2024–2030)**

(A) Projected cell cost per kWh (USD/kWh) for representative cell formats, grouped by cathode chemistry (NMC pouch and cylindrical vs. LFP prismatic). (B) Estimated cost of cells in the commercial battery packs (USD), excluding non-cell components (e.g., module hardware, thermal management, electronics). Projections are based on cost data reported by Orangi et al.<sup>102</sup>

chemistries remain limited by the excessive cost of critical metals, which constrains their potential for comparable cost-reduction rates despite ongoing process improvements.

In automotive applications, the target energy of a battery pack is predetermined by platform constraints, mass limits, and vehicle positioning. Cell selection therefore takes place within a fixed energy window that the pack must deliver. When transitioning from cost at cell level to the cost of the cell set required to reach the target pack energy, the chemistry-driven cost trend becomes markedly more pronounced, since the total number of cells needed is constrained by the pack's predefined architecture. In this context, cell chemistry and format exert a stronger influence on the effective cost of the cell content in the pack and, as shown in Figure 10B, the advantages of LFP chemistries become evident: the prismatic format consistently emerges as the lowest-cost solution, driven by its fewer individual cells requirement, higher nominal energy per cell, low material cost, and efficient pack integration. Conversely, battery packs based on NMC cells (Model Y and Cybertruck) remain the most expensive. This disparity is primarily attributed to the elevated cost per kWh of energy delivered, which stems from both the smaller cell capacity and the higher electrode material cost of NMC cathodes, and the

greater numbers of cells to meet the same energy requirement. In fact, despite similar total energy contents (60.5 kWh for BYD Atto 3 and 71.5 kWh for Tesla Model Y), the resulting pack cost for the NMC format remains significantly higher throughout the forecasted period.

Table 3 provides a direct visualization of the advantages and limitations of the individual cell formats when integrated into the battery pack.

This study investigates lithium-ion cell formats across multiple scales, from cell-to pack-level, evaluating their performance, manufacturability, and cost, to identify format-specific advantages. Unlike prior studies focused on isolated aspects, this work adopts a cross-sectional approach, recognizing that these characteristics collectively impact system-level outcomes. An excessive focus on the single cell may therefore lead to misleading conclusions in the context of automotive integration and technological evolution.

A key trend in the battery industry is the dual evolution of two design strategies: the upscaling of LFP cells into large-format “blade” architectures, and the internal optimization of NMC cylindrical formats such as the 4680 and Cybercell. While both aim to improve energy density and production efficiency, they differ significantly in terms of cost and system integration.

**Table 3. Pack-level advantages, format-specific limitations, and cost**

Pack Type	Format Pros	Format Cons	Cost
Tesla Model Y (NMC 4680)	high gravimetric energy density	cylindrical cooling/structural constraints	medium–high
Tesla Cybertruck (NMC 4680 Gen 2)	high gravimetric and volumetric energy density	very high pack mass; demanding thermal/structural management	high
BYD Atto 3 (LFP Blade)	optimized for CTP integration; improved thermal management	low nominal energy; moderate layout flexibility	low
Tesla Model 3 (LFP prismatic)	straightforward modules; thermal uniformity	lower energy density	low
Mercedes CLA 200 (LFP prismatic)	rigid casing simplifies integration; thermal uniformity	low energy density; limited specific power	low
VW ID.3 (NMC pouch)	efficient packing due to flexible geometry	require external compression frames and edge protection	medium–high

Cost analysis based on the model by Orangi et al.,<sup>102</sup> which shows that high-energy density formats do not necessarily lead to economically efficient solutions. NMC cylindrical cells, despite their high gravimetric energy density and modularity, have lower nominal energy and higher integration overhead, resulting in elevated pack-level costs in volume-constrained applications. In contrast, blade-format LFP cells, though less energy dense, benefit from simpler geometry and lower material costs, enabling the most affordable pack configurations.

This divergence introduces a crucial dynamic in the evolution of lithium-ion technologies: cost differences actively shape technological trajectories. When a format offers substantial cost advantages, it attracts greater industrial interest, faster process refinement, and wider adoption. Cost thereby operates as a technological accelerator, determining which architectures receive the most engineering investment and optimization. Mechanical simplicity, intrinsic safety, and competitive material cost of LFP blade cells, combined with rising production volumes, make them strong candidates for large-scale standardization and automated manufacturing, making them a compelling solution for mainstream electric vehicles and other volume-sensitive applications. As the industry moves toward large-scale electrification, success will strongly depend on cost-efficiency, manufacturability, and integration potential. Formats that align with all these factors, rather than excelling in one alone, are expected to define the next design of lithium-ion batteries. Blade-format cells appear particularly suited to meet these requirements.

## METHODS

This chapter outlines the methodologies adopted for analyzing and comparing lithium-ion battery cell formats, focusing on their geometric, volumetric, and assembly characteristics. This work moves beyond theoretical comparisons by reconstructing 3D models from teardown-based data, offering a high-fidelity and assumption-free benchmarking framework. The development of precise 3D models for volume analysis, and the evaluation of manufacturing processes are explained. Additionally, the study explores the integration of cells into the battery pack and examines their performance. The research concludes with a comparative analysis aimed at identifying technological trends

and providing insights into optimizing battery systems for automotive applications.

## Methodological framework for parameter selection

In the comparative assessment of lithium-ion cell formats, the methodological approach was shaped by the type and quality of information that can be consistently reconstructed across all chemistries, geometries, and manufacturing strategies. The focus was therefore placed on parameters that could be derived with high fidelity from teardown-based geometric reconstruction, publicly available specifications, and documented assembly workflows. These include the following: (1) active and inactive volumes, which quantify how each cell allocates space to energy-storing materials, providing a basis for comparing formats with different casings, tabs, and internal layouts; (ii) gravimetric and volumetric energy densities, which capture the combined effect of chemistry and geometry on energy efficiency and are central for assessing the suitability of each format in mass- and volume-constrained systems; (3) nominal voltage, capacity, and resulting pack energy, which define the feasible series-parallel architecture and influence the extent of electrical interconnections, with direct implications for pack complexity and safety; (4) cell assembly process, in which cutting and welding operations in particular serve as an indicator of manufacturing intensity, since each operation corresponds to a dedicated station in automated production environments and strongly affects throughput; (5) cooling interfaces and structural integration, which describe how each cell format can be embedded within a pack, highlighting constraints linked to geometry, thermal paths, and mechanical support; and (6) gravimetric cell-to-pack ratio, which provides a system-level measure of packaging efficiency, showing how much of the pack mass is effectively converted into active material.

Beyond the parameters selected, additional metrics are also strongly influenced by both cell chemistry and format. Fast-charging, for example depends on lithium-ion diffusivity and charge-transfer resistance (typically higher for NMC than LFP chemistries)<sup>104</sup> and on the current-collector geometry, with cylindrical cells benefiting from distributed or full-tab layouts that reduce local current density during high-C charging.<sup>105</sup> Internal resistance and its degradation with cycling vary with electrode design and stacking strategy,<sup>106</sup> but reported data rely on

heterogeneous protocols that prevent cross-format comparison. Thermal behavior is likewise format-dependent: cylindrical cells exhibit longer radial heat-conduction paths, whereas pouch and prismatic cells offer lower thermal resistance and larger heat-exchange surfaces, though they require external compression for uniform heat management.<sup>11,107</sup> A consistent quantitative analysis of these parameters could not be performed, as comparable simulation data and uniform experimental measurements were not available for all six commercial cells. For this reason, in this study they are not included. Thermal aspects are discussed only qualitatively at pack level, focusing on how cooling strategies differ across formats based on teardown evidence.

### Selection of battery cell formats

Six representative cells used in commercial battery packs were chosen for each format, reflecting current market trends and technologies. The cylindrical format included two Tesla 4680 cells, representing first- and second-generation designs, selected due to their high energy density and growing popularity of 46XX format across various manufacturers. For the pouch format, the LG Chem E78 large-sized cell was analyzed, as it is extensively used in EVs, especially in Volkswagen ID Family cars. Among prismatic cells, the study examined the CATL BTF0 and the BYD C49 cells (selected for the distinct electrode arrangement) and the innovative blade cell from BYD, chosen for its unique structural and functional characteristics. Together, these cells capture a diverse range of designs and applications in automotive batteries.

### 3D modeling and volume analysis

Given the challenge in obtaining or accurately determining the net masses of individual components, as in the method employed by Gorsch et al.,<sup>23</sup> we relied on teardown analyses to estimate their volumes. Volumes calculated from cell models provided a common database for all analyzed cells, enabling assumption-free comparisons and avoiding potential artifacts. This analysis involved calculating and categorizing the volumes of individual components, grouping them into two main categories: active volume, where electrochemical charge is accumulated (occupied by the electrode), and inactive volume, occupied by dead components necessary for cell operation but not active in the energy storage process. Indeed, the inactive volume encompasses structural and functional components indispensable to the cell's functionality and mechanical stability. To gain precise insights, each cell's geometry was recreated through detailed 3D CAD models. The process involves the model development based on publicly available technical specifications and patents, complemented by design schematics when accessible. To reconstruct the Tesla 4680 battery model, the data available in the patent<sup>38,41</sup> and the results of the teardown conducted by Ank et al.<sup>14</sup> and Gorsch et al.<sup>23</sup> were used. Regarding the "Cybercell" (second-generation Tesla 4680 battery cell), the analysis was based on test results back from Munro's video<sup>29</sup> and UC San Diego's teardown.<sup>30</sup> For the prismatic cells, the analysis published by Stock et al.<sup>22</sup> on the CATL BTF0 was fundamental, along with BYD C49 cell specifications provided by Battery Design<sup>88</sup> and EV lithium.<sup>108</sup> Finally, BYD patent US20240128565A1<sup>46</sup> and teardown by Hasan et al.<sup>24</sup> was used for the Blade battery cell. The

last LG pouch cell geometrical data are taken from teardown by Günter et al.<sup>19</sup> The volume of individual components has been calculated to provide a detailed breakdown of each component contribution to the total cell volume.

### Cell assembly processes

To evaluate the key characteristics of the automated manufacturing process in relation to cell format, the various assembly operations were analyzed, identifying the major criticalities at each stage. This assessment provides insight into the manufacturability of different cell formats, highlighting how specific design choices impact production efficiency, process complexity, and potential limitations. Understanding these factors is essential for optimizing large-scale manufacturing and ensuring compatibility with highly automated production systems. The analysis focuses on assembly steps, welding and cutting requirements, machinery, and tools essential for production, to determine potential bottlenecks and advantages inherent to each format.

### Comparative analysis and technological trends

The volumetric data obtained from the 3D models, along with insights into assembly processes, have been compared across the selected formats to identify emerging trends. To compare formats with different nominal energy capacities, the number of cutting and welding operations required for each cell type was normalized per kilowatt-hour. Since individual manufacturing operations cannot be meaningfully expressed as fractions, the resulting values were rounded down to the nearest whole number. This ensures that only complete, physically executable operations are considered. This analysis aims to provide actionable insights for future research and development, highlighting the relative volumetric efficiency of different cell designs, the trade-offs between manufacturing complexity and assembly efficiency, and the impact of cell design on the energy density and overall performance of battery packs.

### Battery pack configurations analysis

As the cell operates within an EV, specifically within the battery pack, its performance must be assessed in the context of the complete vehicle system to ensure a meaningful and accurate comparison. It is worth noting that, although not highlighted in this work, the geometry of the battery pack will influence the vehicle's design and dynamics. Examining cells and battery components arrangement, this work aims to show how the complexity of the battery interconnects the electrode architecture with the final vehicle design. The six vehicles and the relative battery packs studied and compared are as follows: Tesla Model Y, Cybertruck and Model 3, BYD Atto 3, Volkswagen ID.3, and Mercedes CLA 200 (2025).

Key metrics from datasheets, such as gravimetric and volumetric energy densities, GCTP ratio, total energy, nominal voltage, and capacity are also evaluated, offering insights into how the different formats influence the overall energy storage capacity and efficiency of the battery pack. The energy density refers to the amount of energy it can store relative to its mass (Wh/kg) and volume (Wh/L).<sup>109</sup> When not declared in available datasheets, the volumetric energy density has been calculated based on the estimated volume of the battery pack. The nominal

voltage of each battery pack is determined by multiplying the nominal voltage of an individual cell (from datasheet) by the number of cells connected in series, as the voltages of series-connected cells sum linearly, while the nominal capacity is obtained by multiplying the nominal capacity by the number of parallel-connected cells, reflecting the additive contribution of parallel elements to the overall capacity. These parameters are critical for quantifying the total nominal energy of the pack, reported by the battery manufacturer, typically expressed in watt-hours (Wh) or kilowatt-hours (kWh), which represents the theoretical maximum energy that the pack can deliver under standard operating conditions, assuming full utilization of its nominal parameters. While useful for comparative and design purposes, it is important to note that the total nominal energy may differ from the actual usable energy due to efficiency losses, operational constraints, and safety margins applied during real-world operation. The GCTP ratio (in %) expresses a measure of how the available space within the battery pack is optimized for energy storage. It is defined as the total mass of all cells to the total mass of the battery pack.<sup>110</sup> This factor provides a direct measure of how much energy can be stored relative to the weight of the pack, offering a critical indicator of overall design optimization, especially in the context of electric vehicle applications where both weight and energy density are tightly constrained.<sup>111</sup> In some of the battery packs analyzed (as specified in the table captions), the cell-to-pack ratio was directly reported in the literature; if unavailable, it has been calculated based on the declared total pack weight, the number of cells, and their individual weight.

### Lithium-ion battery cost trajectories and comparison

To evaluate the economic implications of different lithium-ion cell formats, a cost analysis has been conducted, based on projected production costs as reported by Orangi et al.<sup>102</sup> in their comprehensive techno-economic model for lithium-ion batteries. The study provides forecasted cell costs (calculated per kWh) for multiple cathode chemistries under high-throughput manufacturing assumptions consistent with future gigafactory scenarios. Values from 2024 to 2030 were used as the baseline reference for this work. A graphite-based anode was assumed for all cell chemistries considered. The pack cost was then estimated scaling the cost at cell level to pack level considering the overall nominal energy but excluding auxiliary components due to a lack of specific data. The cost analysis is therefore anchored to the cell chemistry. While subsystems such as the BMS, thermal interfaces, and structural components remain essential contributors, their relative impact is smaller and exhibits less variability across platforms. The data we found in the literature provided by Frith et al.<sup>112</sup> show that for different battery packs and cell chemistries, the cost of cells constitutes the dominant share of total pack cost. Consequently, the strong cost signal originating from the cells enables the identification of a robust trend in pack-level cost evolution, allowing meaningful comparisons between chemistries.

### RESOURCE AVAILABILITY

#### Lead contact

Requests for further information and resources should be directed to and will be fulfilled by the lead contact, Marella De Santis ([marella.desantis2@unibo.it](mailto:marella.desantis2@unibo.it)).

### Materials availability

This study did not generate new, unique reagents.

### Data and code availability

- Generated data on geometry-derived volume breakdowns and pack-level volumetric energy density reported in this paper will be shared by the [lead contact](#) upon request.
- This paper does not report original code.
- Any additional information required to reanalyze the data reported in this paper is available from the [lead contact](#) upon request.

### ACKNOWLEDGMENTS

The authors thank the Coesia Engineering Center for its valuable support and supervision throughout this work. Their deep expertise in automation and industrial machinery provided essential guidance and significantly contributed to the successful development of this research.

### AUTHOR CONTRIBUTIONS

Conceptualization, M.D.S., I.G., and F.P.; investigation, M.D.S. and F.P.; writing – original draft, M.D.S. and I.G.; writing – review & editing, M.D.S.; supervision, L.P. and A.L.

### DECLARATION OF INTERESTS

The authors declare no competing interests.

### SUPPLEMENTAL INFORMATION

Supplemental information can be found online at <https://doi.org/10.1016/j.xcrp.2026.103162>.

Received: August 6, 2025

Revised: December 11, 2025

Accepted: February 6, 2026

Published: March 10, 2026

### REFERENCES

1. Jaguemont, J., Boulon, L., and Dubé, Y. (2016). A comprehensive review of lithium-ion batteries used in hybrid and electric vehicles at cold temperatures. *Appl. Energy* 164, 99–114.
2. Capasso, C., and Veneri, O. (2014). Experimental analysis on the performance of lithium based batteries for road full electric and hybrid vehicles. *Appl. Energy* 136, 921–930.
3. Li, J., Fleetwood, J., Hawley, W.B., and Kays, W. (2022). From Materials to Cell: State-of-the-Art and Prospective Technologies for Lithium-Ion Battery Electrode Processing. *Chem. Rev.* 122, 903–956.
4. Zubi, G., Dufo-López, R., Carvalho, M., and Pasaoglu, G. (2018). The lithium-ion battery: State of the art and future perspectives. *Renew. Sustain. Energy Rev.* 89, 292–308.
5. Barré, A., Deguilhem, B., Grolleau, S., Gérard, M., Suard, F., and Riu, D. (2013). A review on lithium-ion battery ageing mechanisms and estimations for automotive applications. *J. Power Sources* 241, 680–689.
6. Golubkov, A.W., Scheikl, S., Planteu, R., Voitic, G., Wiltse, H., Stangl, C., Fauler, G., Thaler, A., and Hacker, V. (2015). Thermal runaway of commercial 18650 Li-ion batteries with LFP and NCA cathodes – impact of state of charge and overcharge. *RSC Adv.* 5, 57171–57186.
7. Wang, Q., Ping, P., Zhao, X., Chu, G., Sun, J., and Chen, C. (2012). Thermal runaway caused fire and explosion of lithium ion battery. *J. Power Sources* 208, 210–224.
8. Finegan, D.P., Zhu, J., Feng, X., Keyser, M., Ulmefors, M., Li, W., Bazant, M.Z., and Cooper, S.J. (2021). The Application of Data-Driven Methods



- and Physics-Based Learning for Improving Battery Safety. *Joule* 5, 316–329.
9. Schröder, R., Aydemir, M., and Seliger, G. (2017). Comparatively Assessing different Shapes of Lithium-ion Battery Cells. *Procedia Manuf.* 8, 104–111.
10. Warner, J. (2015). *The Handbook of Lithium-Ion Battery Pack Design* (Elsevier).
11. Baazouzi, S., Feistel, N., Wanner, J., Landwehr, I., Fill, A., and Birke, K.P. (2023). Design, Properties, and Manufacturing of Cylindrical Li-Ion Battery Cells—A Generic Overview. *Batteries* 9, 309.
12. Berg, H. (2015). *Batteries for Electric Vehicles: Materials and Electrochemistry* (Cambridge University Press).
13. Landini, S., Leworthy, J., and O'Donovan, T.S. (2019). A Review of Phase Change Materials for the Thermal Management and Isothermalisation of Lithium-Ion Cells. *J. Energy Storage* 25, 100887. <https://doi.org/10.1016/j.est.2019.100887>.
14. Ank, M., Sommer, A., Abo Gamra, K., Schöberl, J., Leeb, M., Schachtl, J., Streidel, N., Stock, S., Schreiber, M., Bilfinger, P., et al. (2023). Lithium-Ion Cells in Automotive Applications: Tesla 4680 Cylindrical Cell Tear-down and Characterization. *J. Electrochem. Soc.* 170, 120536.
15. Li, S., Marzook, M.W., Zhang, C., Offer, G.J., and Marinescu, M. (2023). How to enable large format 4680 cylindrical lithium-ion batteries. *Appl. Energy* 349, 121548.
16. Halimah, P.N., Rahardian, S., and Budiman, B.A. (2019). Battery Cells for Electric Vehicles. *Int. J. Sustain. Trans. Technol.* 2, 54–57.
17. Pistoia, G. (2013). *Lithium-Ion Batteries: Advances and Applications* (Newnes).
18. Fraunhofer (2022). Development Perspectives for Lithium-Ion Battery Cell Formats. [https://www.isi.fraunhofer.de/content/dam/isi/dokumente/cct/2022/Development\\_perspectives\\_for\\_lithium-ion\\_battery\\_cell\\_formats\\_Fraunhofer\\_2022.pdf](https://www.isi.fraunhofer.de/content/dam/isi/dokumente/cct/2022/Development_perspectives_for_lithium-ion_battery_cell_formats_Fraunhofer_2022.pdf).
19. Günter, F.J., and Wassiliadis, N. (2022). State of the Art of Lithium-Ion Pouch Cells in Automotive Applications: Cell Teardown and Characterization. *J. Electrochem. Soc.* 169, 030515.
20. Meng, Q., Huang, Y., Li, L., Wu, F., and Chen, R. (2024). Smart batteries for powering the future. *Joule* 8, 344–373.
21. Heubner, C., Voigt, K., Marcinkowski, P., Reuber, S., Nikolowski, K., Schneider, M., Partsch, M., and Michaelis, A. (2021). From Active Materials to Battery Cells: A Straightforward Tool to Determine Performance Metrics and Support Developments at an Application-Relevant Level. *Adv. Energy Mater.* 11, 2102647.
22. Stock, S., Hagemeister, J., Grabmann, S., Kriegler, J., Keilhofer, J., Ank, M., Dickmanns, J.L., Schreiber, M., Konwitschny, F., Wassiliadis, N., et al. (2023). Cell teardown and characterization of an automotive prismatic LFP battery. *Electrochim. Acta* 471, 143341.
23. Gorsch, J., Schneiders, J., Frieges, M., Kisseler, N., Klohs, D., Heimes, H., Kampker, A., Muñoz Castro, M., and Siebecke, E. (2025). Contrasting a BYD Blade prismatic cell and Tesla 4680 cylindrical cell with a teardown analysis of design and performance. *Cell Rep. Phys. Sci.* 6, 102453.
24. Hasan, S., Islam, M.S., Bashar, S.M.A., Tamzid, A.A.N., Hossain, R.B., Haque, M.A., and Faishal, R. (2023). Beyond Lithium-Ion: The Promise and Pitfalls of BYD's Blade Batteries for Electric Vehicles. *E3S Web of Conf.* 469, 00005.
25. Kovachev, G., Schrötnner, H., Gstrein, G., Aiello, L., Hanzu, I., Wilkening, H.M.R., Foitzik, A., Wellm, M., Sinz, W., and Ellersdorfer, C. (2019). Analytical Dissection of an Automotive Li-Ion Pouch Cell. *Batteries* 5, 67.
26. Mikolajczak, C., Kahn, M., White, K., and Long, R.T. (2011). *Lithium-Ion Batteries Hazard and Use Assessment Final Report*. <https://www.nrc.gov/docs/ml1719/ml1719a294.pdf>.
27. Pegel, H., Wycisk, D., and Sauer, D.U. (2023). Influence of cell dimensions and housing material on the energy density and fast-charging performance of tabless cylindrical lithium-ion cells. *Energy Storage Mater.* 60, 102796.
28. Pegel, H., Grimm, A., Frey, C., Seefeldt, V., Baazouzi, S., and Sauer, D.U. (2024). Manufacturing of tabless cylindrical lithium-ion cells: Quantifying the influence of cell dimensions and housing material via process-based cost modeling. *J. Energy Storage* 98, 112863.
29. Munro Live. Inside the Cybercell! Tesla Cybertruck 4680 Battery Tear-down. <https://youtu.be/Ig8rdcOAaX4>.
30. The Limiting Factor. Generation 2 4680 Tested/Results & Analysis. <https://www.youtube.com/watch?v=UgFRAzOBb9A>.
31. Nigel. Tesla 4680 Cell Generation 2. <https://www.batterydesign.net/tesla-4680-cell-generation-2/>.
32. Novità sulla batteria 4680 Gen 2 di Tesla. <https://www.nonsolotesla.it/2024/08/19/novita-sulla-batteria-4680-gen-2-di-tesla/>.
33. Waldmann, T., Scurtu, R.-G., Richter, K., and Wohlfahrt-Mehrens, M. (2020). 18650 vs. 21700 Li-ion cells – A direct comparison of electrochemical, thermal, and geometrical properties. *J. Power Sources* 472, 228614.
34. Börner, M.F., Mohsseni, A.M., De, N., Faber, M., Krause, F., Li, W., Bihn, S., Ringbeck, F., and Sauer, D.U. (2024). Manufacturing cost comparison of tabless vs. standard electrodes for cylindrical lithium-ion batteries. *J. Energy Storage* 77, 109941.
35. Knoche, T., Surek, F., and Reinhart, G. (2016). A Process Model for the Electrolyte Filling of Lithium-ion Batteries. *Proced. CIRP* 41, 405–410.
36. Knoche, T., Zinth, V., Schulz, M., Schnell, J., Gilles, R., and Reinhart, G. (2016). In situ visualization of the electrolyte solvent filling process by neutron radiography. *J. Power Sources* 331, 267–276.
37. Ghasemi Yeklangi, A., Ghafari, A., Asgari Sima, F., and Akbari, S. (2024). Advancing lithium-ion battery manufacturing: novel technologies and emerging trends. *J. Appl. Electrochem.* 54, 2653–2682.
38. Tsuruta, K., Dermer, M.E. and Dhiman, R. (2023). Cell with a tabless electrode. Patent application WO2020096973A1. filed November 4, 2019 and published May 14, 2021.
39. Li, S., Kirkaldy, N., Zhang, C., Gopalakrishnan, K., Amietszajew, T., Diaz, L.B., Barreras, J.V., Shams, M., Hua, X., Patel, Y., et al. (2021). Optimal cell tab design and cooling strategy for cylindrical lithium-ion batteries. *J. Power Sources* 492, 229594.
40. Heimes, H., Kampker, A., Lienemann, C. and Locke, M. (2019). *Lithium-Ion Battery Cell Production Process*. (VDMA Battery Production).
41. Eggleston, B., Moors, M., Kalt, A., Grossman, M. and Macnaughton, D. (2022). Tabless energy storage devices and methods of manufacturing. Patent WO2022061187A1. filed September 17, 2021 and published March 24, 2022.
42. Wu, W., Wang, G., Wang, X., Pang, T., Qiu, J., and Guo, T. (2023). Structural Design and Analysis of Battery Cell Winding Machine. *Academic Journal of Science and Technology* 8, 95–99.
43. Chen, H., and Ni, J. (2023). Li-Ion Battery Electrode Manufacturing Control System in Winding Process: Tension Control in Industrial Complex Roll-to-Roll Winding Machine Via SMC-FLC Hybrid Control Method. *J. Manuf. Sci. Eng.* 145, 111007.
44. Sadeghian, A., and Iqbal, N. (2022). A review on dissimilar laser welding of steel-copper, steel-aluminum, aluminum-copper, and steel-nickel for electric vehicle battery manufacturing. *Opt. Laser Technol.* 146, 107595.
45. Kazim, A.L., and Syed, R. (2017). Experimental Characterization of Li-Ion Battery Cells for Thermal Management in Heavy Duty Hybrid Applications (Chalmers University of Technology). <https://hdl.handle.net/20.500.12380/252994>.
46. He, L. (2019). Battery pack, vehicle, and energy storage device. China patent CN110165118A. filed June 19, 2019 and published August 23, 2019.
47. Nigel. CATL BTF0 161Ah LFP. <https://www.batterydesign.net/catl-btf0-161ah-lfp/>.
48. Kokozinski, L., Wieskamp, J., Plumeyer, J.F., Deng, S., Krüger, G., and Wessel, S. (2024). Influence of product characteristics of prismatic

lithium-ion battery cells on the production processes and plant technology for cell finishing. *Proced. CIRP* 130, 462–469.

49. Prismatic Cells. <https://www.batterydesign.net/battery-cell/formats/prismatic-cells/>.
50. Weydanz, W.J., Reisenweber, H., Gottschalk, A., Schulz, M., Knoche, T., Reinhart, G., Masuch, M., Franke, J., and Gilles, R. (2018). Visualization of electrolyte filling process and influence of vacuum during filling for hard case prismatic lithium ion cells by neutron imaging to optimize the production process. *J. Power Sources* 380, 126–134.
51. Heimes, H., Kampker, A., Wennemar, S., Plocher, L., Bockey, G., Michaelis, S., Schüttrumpf, J. Production Process of a Lithium-Ion Battery Cell. 4th Ed. [https://vdma-industryguide.com/fileadmin/battprod/downloads/Production\\_Process\\_of\\_a\\_Lithium-Ion\\_Battery\\_Cell.pdf](https://vdma-industryguide.com/fileadmin/battprod/downloads/Production_Process_of_a_Lithium-Ion_Battery_Cell.pdf) (2023).
52. Kwade, A., Haselrieder, W., Leithoff, R., Modlinger, A., Dietrich, F., and Droeder, K. (2018). Current status and challenges for automotive battery production technologies. *Nat. Energy* 3, 290–300.
53. Kurfer, J., Westermeier, M., Tammer, C., and Reinhart, G. (2012). Production of large-area lithium-ion cells – Preconditioning, cell stacking and quality assurance. *CIRP Ann.* 61, 1–4.
54. Liu, Y., Zhang, R., Wang, J., and Wang, Y. (2021). Current and future lithium-ion battery manufacturing. *iScience* 24, 102332.
55. Wu, B., Yang, Y., Liu, D., Niu, C., Gross, M., Seymour, L., Lee, H., Le, P.M.L., Vo, T.D., Deng, Z.D., et al. (2019). Good Practices for Rechargeable Lithium Metal Batteries. *J. Electrochem. Soc.* 166, A4141–A4149.
56. Gyenes, B., Stevens, D.A., Chevrier, V.L., and Dahn, J.R. (2015). Understanding Anomalous Behavior in Coulombic Efficiency Measurements on Li-Ion Batteries. *J. Electrochem. Soc.* 162, A278–A283.
57. Fath, J.P., Alsheimer, L., Storch, M., Stadler, J., Bandlow, J., Hahn, S., Riedel, R., and Wetzel, T. (2020). The influence of the anode overhang effect on the capacity of lithium-ion cells – a 0D-modeling approach. *J. Energy Storage* 29, 101344.
58. Lee, D. (2018). Investigation of Physical Phenomena and Cutting Efficiency for Laser Cutting on Anode for Li-Ion Batteries. *Appl. Sci.* 8, 266.
59. Schilling, A., Schmitt, J., Dietrich, F., and Dröder, K. (2016). Analyzing Bending Stresses on Lithium-Ion Battery Cathodes induced by the Assembly Process. *Energy Tech.* 4, 1502–1508.
60. Kumar, N., Pamarthi, V.V., and Das, A. (2024). Investigating laser and ultrasonic welding of pouch cell multi-foil current collectors for electric vehicle battery fabrication. *Int. J. Adv. Manuf. Technol.* 134, 2497–2511.
61. Ma, B., Gao, X., Huang, Y., Gao, P.P., and Zhang, Y. (2023). A review of laser welding for aluminium and copper dissimilar metals. *Opt. Laser Technol.* 167, 109721.
62. Yang, P., Chen, X., Li, Y., Gu, M., and Yue, J. (2021). Case of battery, battery, power consuming apparatus, and method and apparatus for manufacturing battery. US patent US20230238610A1. filed March 31, 2023 and published July 27, 2023.
63. Son, S.-B., Robertson, D., Tsai, Y., Trask, S., Dunlop, A., and Bloom, I. (2020). Systematic Study of the Cathode Compositional Dependency of Cross-Talk Behavior in Li-Ion Battery. *J. Electrochem. Soc.* 167, 160508.
64. Xu, C., Fan, Z., Zhang, M., Wang, P., Wang, H., Jin, C., Peng, Y., Jiang, F., Feng, X., and Ouyang, M. (2023). A comparative study of the venting gas of lithium-ion batteries during thermal runaway triggered by various methods. *Cell Rep. Phys. Sci.* 4, 101705.
65. Hummes, D.N., Hunt, J., Hervé, B.B., Schneider, P.S., and Montanari, P.M. (2023). A comparative study of different battery geometries used in electric vehicles. *Lat. Am. J. Energy Res.* 10, 94–114.
66. Mayer, D., and Fleischer, J. (2021). Concept for modelling the influence of electrode corrugation after calendaring on stacking accuracy in battery cell production. *Proced. CIRP* 104, 744–749.
67. Das, A., Li, D., Williams, D., and Greenwood, D. (2018). Joining Technologies for Automotive Battery Systems Manufacturing. *World Electr. Vehic. J.* 9, 22.
68. Kraft, L., Zünd, T., Schreiner, D., Wilhelm, R., Günter, F.J., Reinhart, G., Gasteiger, H.A., and Jossen, A. (2021). Comparative Evaluation of LMR-NCM and NCA Cathode Active Materials in Multilayer Lithium-Ion Pouch Cells: Part II. Rate Capability, Long-Term Stability, and Thermal Behavior. *J. Electrochem. Soc.* 168, 020537.
69. Zwicker, M.F.R., Moghadam, M., Zhang, W., and Nielsen, C.V. (2020). Automotive battery pack manufacturing – a review of battery to tab joining. *Journal of Advanced Joining Processes* 1, 100017.
70. Li, B., Xiao, J., Zhu, X., Wu, Z., Zhang, X., Han, Y., Niu, J., and Wang, F. (2024). Enabling high-performance lithium iron phosphate cathodes through an interconnected carbon network for practical and high-energy lithium-ion batteries. *J. Colloid Interface Sci.* 653, 942–948.
71. Wang, B., Redondo, E., Le Fevre, L.W., Brookfield, A., McInnes, E.J.L., and Dryfe, R.A.W. (2025). Evolution of LiNi<sub>0.8</sub>Mn<sub>0.1</sub>Co<sub>0.1</sub>O<sub>2</sub> (NMC811) Cathodes for Li-Ion Batteries: An In Situ Electron Paramagnetic Resonance Study. *J. Phys. Chem. C Nanomater. Interfaces* 129, 7667–7676.
72. Ohneseit, S., Finster, P., Floras, C., Lubenau, N., Uhlmann, N., Seifert, H.J., and Ziebert, C. (2023). Thermal and Mechanical Safety Assessment of Type 21700 Lithium-Ion Batteries with NMC, NCA and LFP Cathodes—Investigation of Cell Abuse by Means of Accelerating Rate Calorimetry (ARC). *Batteries* 9, 237.
73. Kim, J., and Cho, B.H. (2013). Screening process-based modeling of the multi-cell battery string in series and parallel connections for high accuracy state-of-charge estimation. *Energy* 57, 581–599.
74. Nigel. 2022 Tesla Model Y 4680. [https://www.batterydesign.net/2022-tesla-model-y-4680/\(2022\)](https://www.batterydesign.net/2022-tesla-model-y-4680/(2022)).
75. Munro Live. Tesla's Battery Evolution: 4680 vs 2170 Cell Comparison. <https://www.youtube.com/watch?v=c7qel8tjHMs4>.
76. Munro Live. 4680 Battery Pack: What We Found Under the Foam! <https://www.youtube.com/watch?v=ozesl3OZEG0>.
77. Nigel. Tesla Cybertruck Battery. <https://www.batterydesign.net/tesla-cybertruck-battery/>.
78. Tesla Cybertruck Battery Pack: Our First Impressions Under the Lid. <https://www.youtube.com/watch?v=ipe5A4ZN3Gc>.
79. Battery Cell Configuration & Model Y Comparisons: Inside the Tesla Cybertruck Battery Pack. [https://www.youtube.com/watch?v=x25KU\\_wxxWw](https://www.youtube.com/watch?v=x25KU_wxxWw).
80. BYD Atto 3 battery dismantle P2 - contactor block. <https://www.youtube.com/watch?v=wD7R8xPHckM&list=PLif0c5zH6aQruU84dcCle5KomvQRmQgB&index=3>.
81. BYD Atto 3 battery dismantle P1.5 - Whoops. <https://www.youtube.com/watch?v=j4dbk8DG0o8&list=PLif0c5zH6aQruU84dcCle5KomvQRmQgB&index=2>.
82. BYD Atto 3 battery to home storage P5 - BMS cell taps. <https://www.youtube.com/watch?v=w2uZ-Q378pQ&list=PLif0c5zH6aQruU84dcCle5KomvQRmQgB&index=8>.
83. BYD Atto 3 battery dismantle P1. <https://www.youtube.com/watch?v=HPTefsQNGI4&list=PLif0c5zH6aQruU84dcCle5KomvQRmQgB&index=1>.
84. Tesla LFP Model 3. <https://www.batterydesign.net/tesla-lfp-model-3/>.
85. Tesla Model 3 LFP Battery. [https://www.youtube.com/watch?v=mZZy\\_6O41sl](https://www.youtube.com/watch?v=mZZy_6O41sl).
86. Tesla Battery Teardown - Model 3 Standard Range Plus. <https://www.youtube.com/watch?v=8Wamu0hyngU>.
87. Tesla Model 3 - Cooling System Overview. <https://www.youtube.com/watch?v=vGfXyLLaO7I>.
88. Mercedes MMA Battery. <https://www.batterydesign.net/mercedes-mma-battery/>.
89. Dhage, A. Volkswagen MEB Battery Pack ID Family. <https://www.batterydesign.net/volkswagen-meb-battery-pack-id-family/>.
90. Open up a VW id3 id4 lithium battery module. <https://www.youtube.com/watch?v=uP-iOsd4cVY>.

91. 2021 VW ID.3 BATTERY TEARDOWN | WHATS INSIDE THE MEB BATTERY? ALEX TECH TIME #6 | ESDI EV. <https://www.youtube.com/watch?v=twgNqutgFt4&t=3s>.
92. Dhage, A. VW Benchmarking ID 3, 4, 5 and Buzz. <https://www.batterydesign.net/vw-benchmarking-id3-id4-id5-and-id-buzz/>.
93. Sumpf, R.D., Jr., Stockton, W.B., Spooner, C., Prodan, C., Gorasia, J.B., Harris, K., Burke, D., Szafer, D.G., Patel, K., Parker, B., et al. (2021). Integrated energy storage system. Patent WO2021102340A1. filed November 20, 2020 and published May 27, 2021.
94. Grace, D., Goldman, M., Phillips, W., West, DW, Guerra, P., Rittenburg, AW, Singh, G., Anderson, K., Horton, A., How, P., et al. (2016). Self-activated draining system. US patent US9293792B2. filed May 10, 2013 and published March 22, 2016.
95. BYD Blade. <https://www.batterydesign.net/byd-blade/>.
96. BYD ATTO 3 Specification. <https://www.byd.com/content/dam/byd-site/en-be/product/atto3/BYD%20ATTO%203.pdf>.
97. Nuova CLA elettrica. Mercedes-Benz. [https://www.mercedes-benz.it/passengercars/models/saloon/cla-electric/overview.html?abtest-new\\_cta\\_print=control#features-ricarica](https://www.mercedes-benz.it/passengercars/models/saloon/cla-electric/overview.html?abtest-new_cta_print=control#features-ricarica).
98. Vw id3 id4 battery thermal management. <https://www.youtube.com/watch?v=XpXuZYsyRcw>.
99. L  bberding, H., Wessel, S., Offermanns, C., Kehr  r, M., R  ther, J., Heimes, H., and Kampker, A. (2020). From Cell to Battery System in BEVs: Analysis of System Packing Efficiency and Cell Types. *World Electr. Vehic. J.* 11, 77.
100. Das, U.K., Shrivastava, P., Tey, K.S., Bin Idris, M.Y.I., Mekhilef, S., Jamei, E., Seyedmahmoudian, M., and Stojcevski, A. (2020). Advancement of lithium-ion battery cells voltage equalization techniques: A review. *Renew. Sustain. Energy Rev.* 134, 110227.
101. Baek, D., Bocca, A., and Macii, A. (2022). A cost of ownership analysis of batteries in all-electric and plug-in hybrid vehicles. *Energy Ecol. Environ.* 7, 604–613.
102. Orangi, S., Manjong, N., Clos, D.P., Usai, L., Burheim, O.S., and Str  mman, A.H. (2024). Historical and prospective lithium-ion battery cost trajectories from a bottom-up production modeling perspective. *J. Energy Storage* 76, 109800.
103. Mauler, L., Duffner, F., Zeier, W.G., and Leker, J. (2021). Battery cost forecasting: a review of methods and results with an outlook to 2050. *Energy Environ. Sci.* 14, 4712–4739.
104. Yeganehdoust, F., Madikere Raghunatha Reddy, A.K., and Zaghib, K. (2025). Cell Architecture Design for Fast-Charging Lithium-Ion Batteries in Electric Vehicles. *Batteries* 11, 20.
105. Pegel, H., Wycisk, D., Scheible, A., Tenders, L., Latz, A., and Sauer, D.U. (2023). Fast-charging performance and optimal thermal management of large-format full-tab cylindrical lithium-ion cells under varying environmental conditions. *J. Power Sources* 556, 232408.
106. Bridgewater, G., Capener, M.J., Brandon, J., Lain, M.J., Copley, M., and Kendrick, E. (2021). A Comparison of Lithium-Ion Cell Performance across Three Different Cell Formats. *Batteries* 7, 38.
107. Li, W., Xia, Y., Chen, G., and Sahraei, E. (2018). Comparative study of mechanical-electrical-thermal responses of pouch, cylindrical, and prismatic lithium-ion cells under mechanical abuse. *Sci. China Technol. Sci.* 61, 1472–1482.
108. BYD C49 100Ah Lithium LiFePO4 Battery Cell. <https://www.evliithium.com/LiFePO4-Battery/byd-100ah-lifepo4-battery.html>.
109. Borah, R., Hughson, F.R., Johnston, J., and Nann, T. (2020). On battery materials and methods. *Mater. Today Adv.* 6, 100046.
110. Koloch, J., Heienbrok, M., Kasperek, M., and Lienkamp, M. (2025). From Cell to Pack: Empirical Analysis of the Correlations Between Cell Properties and Battery Pack Characteristics of Electric Vehicles. *World Electr. Vehic. J.* 16, 484.
111. Nigel. Cell to Pack Mass Ratio. <https://www.batterydesign.net/cell-to-pack-mass-ratio/>.
112. Frith, J.T., Lacey, M.J., and Ulissi, U. (2023). A non-academic perspective on the future of lithium-based batteries. *Nat. Commun.* 14, 420.

**Cell Reports Physical Science, Volume 7**

**Supplemental information**

**Design and production trade-offs  
in lithium-ion batteries from cell formats  
to electric vehicles**

**Marella De Santis, Irene Giusti, Federico Poli, Luca Piancastelli, and Alfredo Liverani**

## SUPPLEMENTAL INFORMATION

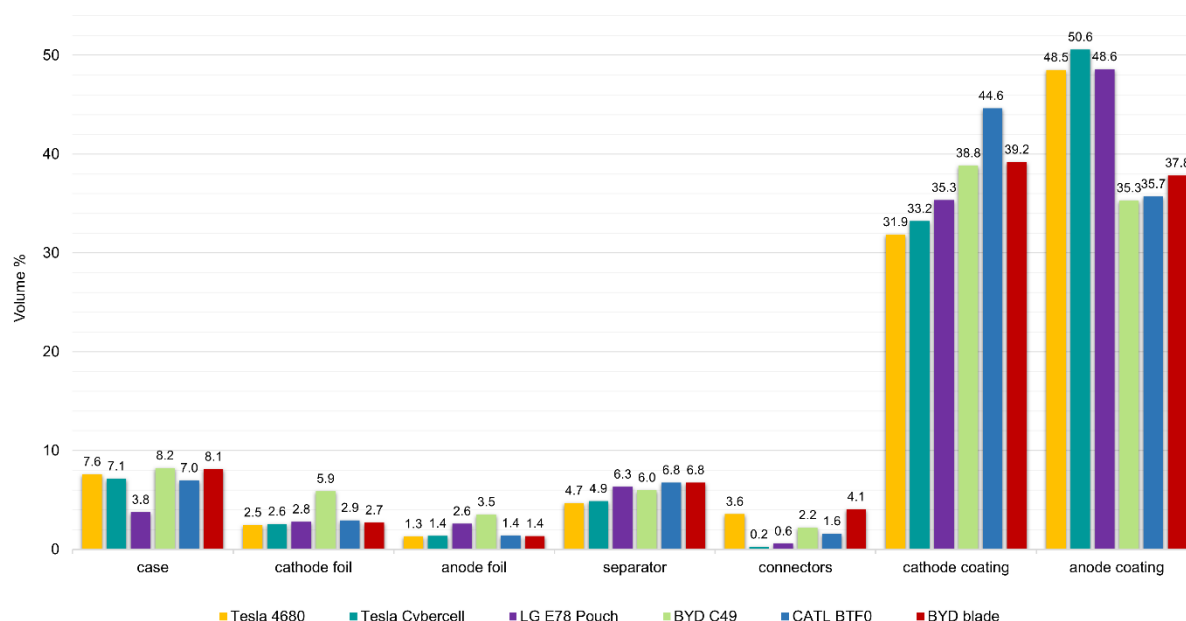


**Figure S1. Volumetric distribution of cell components, showing the contribution of active and inactive materials to overall available internal volume. Values are calculated from teardown-based CAD models of each battery cell.**

Specifications	4680	Cybercell
Nominal Voltage (V)	3.7	3.7
Nominal Capacity (Ah)	23.35	26
Nominal Energy (Wh)	86.5	95.2
Gravimetric Energy Density (Wh/kg)	244	272
Volumetric Energy Density (Wh/L)	643.3	716
Cycle Life	2000	2000
Cathode Chemistry	NMC811	NMC955

All data are taken from manufacturer data and literature sources <sup>31,77</sup>.

**Table S1. Cylindrical cells metrics and specifications.**

Metrics	4680	Cybercell
Diameter (mm)	46	46
Height (mm)	80	80
Can thickness (mm)	0.6	0.35
Cu tab disk thickness (mm)	0.2	-
Cu tab disk diameter (mm)	44	-
Al tab disk thickness (mm)	0.2	0.1
Al tab disk diameter (mm)	40	40
Plastic disk thickness (mm)	0.65	-
Volume (L)	0.133	0.133
Mass (kg)	0.355	0.35
Can shell weight (g)	70	49

All data are taken from public teardown and literature sources <sup>14,23,29–32,77</sup>.

**Table S2. Differences in geometry, cell architecture and components of cylindrical cells.**



Component	4680 Vol*	4680 Vol %	Cybercell Vol*	Cybercell Vol %	Delta V (%)
Case	8738	7.60	7881	7.15	-9.8
Cathode foil	2826	2.46	2826	2.56	0
Anode foil	1496	1.30	1496	1.36	0
Separator	5379	4.68	5379	4.88	0
Connectors	4100	3.57	300	0.27	-92.7
Cathode coating	36616	31.86	36616	33.21	0
Anode coating	55764	48.52	55764	50.57	0

\*The volume is expressed in mm<sup>3</sup>.

The volume of each component is calculated by the authors from reconstructed CAD models.

**Table S3. Volume distribution in cylindrical cells.**

Specifications	BYD Blade	CATL BTF0	BYD C49
Nominal Voltage (V)	3.2	3.2	3.2
Nominal Capacity (Ah)	135	161	100
Nominal Energy (Wh)	432	515	320
Gravimetric Energy Density (Wh/kg)	160	166	163
Volumetric Energy Density (Wh/L)	424	356	331
Cycle Life	3000+	≥3500	≥6000
Cathode Chemistry	LFP	LFP	LFP

All data are taken from manufacturer data and literature sources <sup>22–24,96,109</sup>.

**Table S4. Prismatic cells metrics and specifications.**

Metrics	BYD Blade	CATL BTF0	BYD C49
Length (mm)	960	280	160
Height (mm)	90	82	121
Width (mm)	12	63	50
Case thickness (mm)	0.3	1	1.1
Electrode sheets/ windings	26 cathode, 27 anode	40 windings, 2 rolls	~ 130*
Volume (L)	1.04	1.4	0.97
Mass (kg)	2.63	3.1	1.96

\*Calculated value from teardown-based CAD model reconstruction.

All data are taken from public teardown and literature sources <sup>22–24,49,96,109</sup>.

**Table S5. Differences in geometry, cell architecture and components of prismatic cells.**

Component	BYD Blade Vol*	BYD Blade Vol %	CATL BTF0 Vol*	CATL BTF0 Vol %	BYD C49 Vol*	BYD C49 Vol %
Case	60000	8.1	78060	6.97	70000	8.2
Cathode foil	24536	2.7	32978	2.94	50000	5.9
Anode foil	12740	1.4	15510	1.38	30000	3.5
Separator	50907	6.8	75675	6.76	90000	6.0
Connectors	30000	4.1	17800	1.59	18720	2.2
Cathode coating	290000	39.2	500000	44.64	300000	38.8
Anode coating	280000	37.8	400000	35.71	330000	35.3

\*The volume is expressed in mm<sup>3</sup>.

The volume of each component is calculated by the authors from reconstructed CAD models.

**Table S6. Volume distribution in prismatic cells.**

Specifications	LG E78 Pouch
Nominal Voltage (V)	3.65
Nominal Capacity (Ah)	78
Nominal Energy (Wh)	289
Gravimetric Energy Density (Wh/kg)	265
Volumetric Energy Density (Wh/L)	609
Cycle Life	≥3000
Cathode Chemistry	NMC712

All data are taken from manufacturer data and literature sources <sup>114,115</sup>.

**Table S7. LG Chem E78 Pouch cell metrics and specifications.**

Metrics	LG Chem E78
Length (mm)	545 mm (535 mm without tabs)
Width (mm)	98 mm
Height (mm)	9.12 mm
Pouch bag thickness (μm)	144
Electrode sheets	18 cathode, 19 anode
Tab cross-section (mm <sup>2</sup> )	22.5
Volume (L)	0.438
Mass (kg)	1.101

All data are taken from public teardown and literature sources <sup>19,25,114</sup>.

**Table S8. Geometric parameters and dimensions of LG Chem E78 pouch cell.**

Component	Volume*	Volume %
Case	17017	3.76
Cathode foil	12663	2.80
Anode foil	11734	2.59
Separator	28662	6.33
Connectors	2600	0.57
Cathode coating	160000	35.35
Anode coating	220000	48.60

\*The volume is expressed in mm<sup>3</sup>

The volume of each component is calculated by the authors from reconstructed CAD models.

**Table S9. Volume distribution in LG Chem E78 pouch cell.**

Metrics	Model Y (4680)	Cybertruck (Cybercell)	Atto 3 (BYD blade)	Model 3 (BTF0)	CLA 200 (BYD C49)	ID 3 (LG E78)
N. Voltage (V)	340.4	710.4	384	339.2	614.4	394.2
N. Capacity (Ah)	210.2	182	135	163.3	100	156
Grav. energy density (Wh/kg)	161	171	145	126	120	162
Vol. energy density (Wh/L)*	150	175	190	127	125	165

\*Volumetric Energy Density is calculated by the authors based on estimated battery pack volume. The data reported in table are from manufacturer data, teardown and literature sources <sup>29,75–93</sup>.

**Table S10. Battery packs metrics.**